

Binary boson stars: Merger dynamics and formation of rotating remnant stars

Nils Siemonsen^{1,2,3,*} and William E. East¹

¹*Perimeter Institute for Theoretical Physics, Waterloo, Ontario N2L 2Y5, Canada*

²*Arthur B. McDonald Canadian Astroparticle Physics Research Institute,*

64 Bader Lane, Queen's University, Kingston, ON K7L 3N6, Canada

³*Department of Physics & Astronomy, University of Waterloo, Waterloo, ON N2L 3G1, Canada*

(Dated: Wednesday 14th June, 2023)

Scalar boson stars have attracted attention as simple models for exploring the nonlinear dynamics of a large class of ultra compact and black hole mimicking objects. Here, we study the impact of interactions in the scalar matter making up these stars. In particular, we show the pivotal role the scalar phase and vortex structure play during the late inspiral, merger, and post-merger oscillations of a binary boson star, as well as their impact on the properties of the merger remnant. To that end, we construct constraint satisfying binary boson star initial data and numerically evolve the nonlinear set of Einstein-Klein-Gordon equations. We demonstrate that the scalar interactions can significantly affect the inspiral gravitational wave amplitude and phase, and the length of a potential hypermassive phase shortly after merger. If a black hole is formed after merger, we find its spin angular momentum to be consistent with similar binary black hole and binary neutron star merger remnants. Furthermore, we formulate a mapping that approximately predicts the remnant properties of any given binary boson star merger. Guided by this mapping, we use numerical evolutions to explicitly demonstrate, for the first time, that rotating boson stars can form as remnants from the merger of two non-spinning boson stars. We characterize this new formation mechanism and discuss its robustness. Finally, we comment on the implications for rotating Proca stars.

I. INTRODUCTION

Gravitational wave (GW) and electromagnetic observations from isolated and binary compact objects can be explained remarkably well by invoking the presence of a black hole, as predicted by general relativity. The black hole paradigm explains physics across several orders of magnitude, from stellar mass compact binary mergers and X-ray binaries, at smaller scales, to active galactic nuclei, at larger scales. However, while these observations require ultracompact central engines, the defining feature of black holes—the event horizon—remains less well tested. Performing the most stringent tests of the black hole paradigm necessitates alternative predictions that can be used to perform model selection with gravitational and electromagnetic observations.

Such considerations have driven the construction of a large class of exotic ultracompact objects mimicking many of the observational features of black hole spacetimes *without* possessing an event horizon (see Ref. [1] for a review). These range from various kinds of fluid stars [2–4], to string theory-inspired ultra compact fuzzballs [5–7]. Lacking horizons, these objects can exhibit distinct relativistic properties, such as stable light rings, isolated ergoregions, and super-extremal spins, that are not present in black hole spacetimes [1], and which can lead to new gravitational phenomenology, including GW echoes [8] and ergoregion instabilities [9], opening a window into the models of quantum gravity and dark matter from which these objects emerge. Leveraging GW

observations to confront the black hole hypothesis, however, requires an understanding of black hole-mimicking objects in the strong-field and highly dynamical regime. While there are numerous ultracompact object models where stationary solutions have been constructed, self-consistently evolving these objects is challenging, or even ill-defined, in many cases.

As a result, scalar boson stars (BSs) have received significant attention as proxies for generic ultracompact black hole mimickers in the strong-field, dynamical regime. First constructed in Refs. [10–12], BSs have been studied extensively in isolation in a variety of models with various scalar self-interactions [13–17]. Analogous to fluid stars, a family of solutions in a particular model contains a single, or pair, of stable branches [18–20]. Stability studies in the linear regime have demonstrated the robustness of non-rotating BS solutions to perturbations [21–27]. Spherically symmetric BSs are consistently formed dynamically from coherent [12, 28] and incoherent [29–32] diffuse initial states, as well as through binary BS mergers in head-on [33–41] and orbiting mergers [40, 42–45], further solidifying their robustness (for a review, see Ref. [16]). Analogous analyses have shown similar dynamical behavior in vector stars, called Proca stars (PSs)¹ [46–50]. While the existence, stability, and formation of spherically symmetric stars from isolated or binary solutions is well-studied, the role of angular momentum in these systems is still poorly understood. It was noticed early on that spherical stars cannot rotate perturbatively [51] (i.e., they are not continuously

* nsiemonsen@perimeterinstitute.ca

¹ Here, we will use BS to refer exclusively to stars made from scalar matter, and PS to refer to those formed from a vector field.

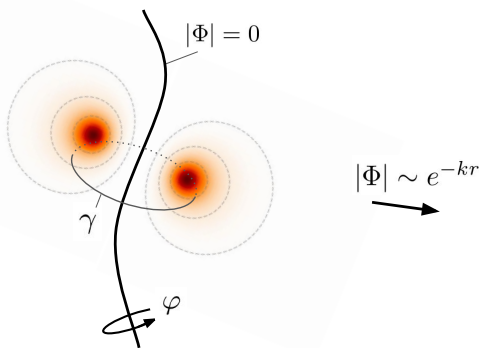


Figure 1. We show schematically an axial slice through a rotating BS at a fixed time. The scalar field magnitude $|\Phi|$ (red/yellow color) vanishes along the central vortex line, attains a maximum value some distance from the vortex line, and drops off exponentially towards large distances $\sim e^{-kr}$, with some $k > 0$. Surfaces of constant scalar field magnitude are indicated as gray dashed lines. Integrating the gradient of the scalar phase $\text{Arg}(\Phi) = \psi$ along the path γ around the vortex in the azimuthal direction φ gives the vortex index q of the rotating BS, as defined in (2).

connected to their non-rotating counterparts; notable exceptions exist in the Newtonian limit [52]). Later it was found that rotating BS (and PS) solutions with quantized angular momentum exist [46, 53, 54]. However, only stars in scalar models with self-interactions are perturbatively stable against a non-axisymmetric instability [55–58]. Lastly, despite numerous efforts to form rotating BSs dynamically [40, 43–45, 59], even in those models with rotating stars without known instabilities [57], no rotating BSs has been formed from the merger of two non-spinning stars. If BSs mergers cannot form a (non-black-hole) rotating remnant, that would seem to place a serious impediment on their ability to mimic black holes without invoking horizons.

BSs are stationary, non-topological solutions of a complex massive scalar field Φ with a global $U(1)$ symmetry minimally coupled to gravity (the generalization of Q-ball solutions to include self-gravity [60, 61]). The tendency of a localized wave solution to disperse is balanced by gravitational attraction, while the gravitational decay of BSs (dissipation through gravitational radiation) is precluded by their conserved $U(1)$ -charge Q , counting the number of bosons in the system. Generally, the scalar field of an isolated BS takes the form

$$\Phi = \phi e^{i(\omega t - m\varphi)}, \quad (1)$$

with magnitude ϕ , frequency ω , integer azimuthal index m , time coordinate t , and azimuthal coordinate φ . For spherical solutions, the scalar field magnitude is maximum at the origin, and exponentially decays towards spatial infinity. Their rotating counterparts with non-zero angular momentum $J = mQ$, on the other hand, exhibit vanishing scalar field magnitude at their centers and are classified by the index $|m| \geq 1$, leading to toroidal sur-

faces of constant scalar field magnitude. Therefore, rotating BSs can also be understood as *vortices* with gravitationally bound scalar matter. This is shown schematically in Figure 1. Within a spacelike slice of a spacetime with scalar field $\Phi = \phi e^{i\psi}$, we define a vortex to be the line L through the hypersurface such that the integral of the gradient of the scalar phase ψ along the oriented loop γ in a sufficiently small neighborhood around L is a non-zero integer q ,

$$\frac{1}{2\pi} \oint_{\gamma} dl_i D^i \psi = q, \quad (2)$$

called the vortex index. Here, D_i is the covariant derivative in the hypersurface. Since for non-spinning BSs the phase ψ is constant in space, i.e., $D^i \psi = 0$, applying this definition gives $q = 0$. In the case of isolated rotating BSs, the gradient $D^i \psi$ is non-trivial. In fact, the vortex line is the line of vanishing $|\Phi|$ through the center of mass of these solutions (as shown in Figure 1). The vortex index q is exactly the azimuthal index m of the star, $|q| = m$. Hence, in the context of these rotating BS solutions, the connection between angular momentum and the vortex index is manifest. Lastly, reversing the orientation of γ implies $q \rightarrow -q$.

The appearance and role of vortices in various contexts have been the subject of extensive study for decades. In particular, quantized vortices are generic features in Bose-Einstein condensates [62], superfluids [63–65], wave-like dark matter [66–69], or cosmic strings [70]; all of which are described by scalar models similar (or identical) to the scalar theories with BS solutions considered here. In these contexts, vortices appear dynamically, for instance, as the result of symmetry breaking phase transitions [70–72], or the introduction of angular momentum into the system [62, 69]. Therefore, from vortex lattices in trapped superfluids to cosmic string networks and spinning dark matter halos, vortices are important in a wide variety of phenomena. Here, we show that vortices, their relation to angular momentum, and the evolution of the phase of the scalar field are also crucial ingredients in understanding and predicting the merger dynamics of binary BSs.

In this work, we numerically evolve the nonlinear Einstein-Klein-Gordon system of equations in 3D to study the role of the scalar field during the late inspiral, merger, and ringdown of spinning and non-spinning binary BSs in different nonlinear scalar models with a global $U(1)$ symmetry. As the scalar interactions are exponentially enhanced with decreasing binary separation, we find that the scalar phase plays a crucial role during the later inspiral and merger of binary BSs. We illustrate some cases where the nature of the endstate of a binary merger is determined by the relative phase of the stars at early times. Secondly, we provide a mapping that approximately predicts the outcome of any given binary (or multi) BS and PS merger. Utilizing this mapping to guide the choice of parameters, we show, for the first time, using numerical evolutions, cases where rotat-

ing BSs form dynamically from a non-spinning binary BS merger. We provide a set of necessary conditions for the formation of these rotating BS and PS remnants and identify the regions in parameter space where this formation channel is expected to be active.

The remainder of the paper is organized as follows. In Sec. II, we briefly review the role of scalar interactions in the dynamics of binary Q-balls, then proceed to apply these results to binary BS inspirals, first qualitatively, and then systematically, in the case of a non-spinning binary inspiral, and finally construct a mapping to approximately predict the remnant properties of any given binary BS inspiral. In Sec. III, we begin by listing the necessary conditions for the formation of a rotating remnant BS from the merger of a non-spinning binary, explicitly demonstrate the formation of a rotating BS remnant by numerically evolving a suitable system, discuss the robustness and other characteristics of this formation channel, and study the remnant resulting from the merger of a spinning BS with a non-spinning BS. In Sec. IV, we further discuss our findings and conclude. Finally, in the appendices, we revisit a non-axisymmetric instability present in rotating BSs in light of our findings, and provide further details on our numerical setup. We use geometric units with $G = c = 1$ throughout.

II. MERGER DYNAMICS

During the merger of two BSs in a nonlinear scalar model, scalar interactions play an important role along with gravitational interactions. Due to the exponential fall-off of the scalar field amplitude at large distances from an isolated star, the scalar forces are also exponentially suppressed for a binary at large separations. Conversely, the scalar field interaction is exponentially enhanced during the later inspiral and merger of two BSs, and is crucial to understanding the merger dynamics.

In Sec. II A, we introduce the nonlinear complex scalar theories considered in this work. Continuing in Sec. II B, we briefly review known results for Q-balls and BSs, and conjecture how these results can be translated to the inspiral and merger dynamics of binary BSs. We apply this intuition to the inspiral of a representative binary BS in Sec. II C, and study the scalar interaction dependence on the scalar phase systematically in the context of a binary BS inspiral in Sec. II D. Lastly, in Sec. II E, we conjecture a mapping that identifies the remnant of any multi BS encounter and illustrate its utility in the context of an inspiraling spinning binary BS. (We also comment on the implications for PSs.)

A. Scalar models

In this work, we mainly consider a complex scalar field Φ whose potential $V(|\Phi|)$ includes both a quadratic term corresponding to a mass μ , as well as higher order contri-

butions from self-interactions. We also consider massive complex vector fields A_μ in select cases in order to compare to the behavior of scalar theories; for details on this and the PS solutions in these models, see Appendix C. The scalar dynamics occurs in a dynamical spacetime $g_{\mu\nu}$ of Ricci curvature scalar R . Therefore, the globally $U(1)$ invariant action is

$$S = \int d^4x \sqrt{-g} \left[\frac{R}{16\pi} - g^{\mu\nu} \nabla_{(\mu} \bar{\Phi} \nabla_{\nu)} \Phi - V(|\Phi|) \right]. \quad (3)$$

Here, and in the following, overbars denote complex conjugation. Scalar self-interactions are classified into *attractive* and *repulsive* potentials. Attractive (repulsive) potentials are those with negative (positive) first correction beyond the mass-term, which means the increasing nonlinear self-interactions, e.g. in a binary BS with decreasing separation, reduce (enhance) the potential energy. We focus on one type of potential for each class and note that similar behavior is expected generally for self-interactions of the same class. The solitonic potential [18]

$$V_{\text{sol}}(|\Phi|) = \mu^2 |\Phi|^2 \left[1 - \frac{2|\Phi|^2}{\sigma^2} \right]^2, \quad (4)$$

is characterized by the coupling constant σ . In the $\sigma \rightarrow \infty$ limit, the self-interactions reduce to the simple massive scalar case with *attractive* higher order corrections: $V_{\text{sol}} = \mu^2 |\Phi|^2 - 4\mu^2 |\Phi|^4 / \sigma^2 + \mathcal{O}(|\Phi|^6)$. In this scalar model, there are ultracompact solutions with stable light rings, even in spherical symmetry [43, 73]. In the flat spacetime limit, this scalar theory admits exact, non-topological, solitonic solutions called Q-balls, which are continuously connected to their self-gravitating cousins, i.e., BSs [53]. The repulsive scalar interactions are represented by

$$V_{\text{rep}}(|\Phi|) = \mu^2 |\Phi|^2 + \lambda |\Phi|^4, \quad (5)$$

with $\lambda > 0$. Both the scalar solitonic and repulsive models (as well as the massive vector model) admit non-trivial, stationary, axisymmetric solutions describing a gravitationally-bound relativistic scalar (or vector) condensate. The details of how these scalar and vector star solutions are obtained from the action (3), and constructed numerically, can be found in Appendix C (for PSs) and in, e.g., Ref. [57] (for BSs). Here, we simply note that in the scalar case the ansatz (1) with asymptotically flat boundary conditions yields an infinite set of families of BS solutions each labeled by their azimuthal number m , and parameterized by their frequency $\omega < \mu$. The spherically symmetric $m = 0$ family of solutions is non-rotating, while the $m \neq 0$ families consist of non-perturbatively rotating stars with *quantized* angular momentum $J = mQ$, where Q is the global $U(1)$ -charge. We define the radius of BS solutions as the circular radius R , within which 99% of the solution's energy is contained, and the compactness C as the ratio of the ADM mass M to radius, $C = M/R$.

B. Scalar interactions

On a flat background, a Q-ball can be decomposed, as in (1), into a spatial profile ϕ and a phase $\omega t - m\varphi \rightarrow \psi$. In the case of an isolated, non-spinning (i.e., $m = 0$) Q-ball, the spatial profile peaks at the center of the solution and decays exponentially as $\phi \sim e^{-kr}$ at large distances r from the center, while the complex phase exhibits a harmonic time dependence $\psi = \omega t$, together with the arbitrary constant phase-shift $\psi \rightarrow \psi + \alpha$, under which the model is symmetric. A binary Q-ball with separation $|\mathbf{x}_1 - \mathbf{x}_2| = D \gg 1/k_i$, with $i = 1$ and 2 , is approximately given by the scalar field profile

$$\Phi \sim e^{i\omega_1 t} \phi_1(\mathbf{x}_1) + e^{i(\omega_2 t + \alpha)} \phi_2(\mathbf{x}_2). \quad (6)$$

The scalar self-interactions lead to momentum exchange—a scalar force—between the two solitons [74–76]. This force ultimately originates from the internal non-stationarity of the complex phase of the scalar field. For the binary defined in (6), the scalar force has a dependence given by [74, 76]

$$\tilde{F} \sim \cos[(\omega_1 - \omega_2)t + \alpha] e^{-D(k_1 + k_2)}, \quad (7)$$

for $1/D \ll k_1, k_2$. The magnitude of \tilde{F} is exponentially suppressed by the distance D between the solitons, while the sign of \tilde{F} is determined by the phase evolution of the binary. This spatial dependence and importance of the complex phase is applicable also in the BS case, as we see below. In the limit of equal frequency, $\omega_1 = \omega_2$, the temporal dependence vanishes, and the sign of \tilde{F} is determined solely by the phase-offset α . In the general case of $\omega_1 \neq \omega_2$, a breathing motion appears in response to the harmonically oscillating force applied on each Q-ball [74], independent of the constant offset α . Therefore, the complex phase dynamics determine the sign of the effective force applied, while the magnitude is exponentially suppressed by the distance between the solitons.

The dynamics of the complex phases ψ_1 and ψ_2 is non-trivial in the presence of nonlinear scalar interactions [75]. Integrating out the spatial degrees of freedom, assuming a large separation, and identical solitons, the evolution follows $\dot{\psi}_1 + \dot{\psi}_2 = 0$ and $\ddot{\psi}_1 - \ddot{\psi}_2 \sim \varepsilon^2 \sin(\psi_1 - \psi_2)$, with the overlap $\varepsilon \sim e^{-D(k_1 + k_2)}$. For the special case of $\psi_1 = \psi_2 + n\pi$, with $n \in \mathbb{Z}$, the evolution trivializes, i.e., $\dot{\psi}_1, \dot{\psi}_2 = \text{const.}$, and the soliton's phase-evolution is set by a single frequency. However, in general, an initial phase-offset $\alpha = (\psi_1 - \psi_2)|_{t=0} \in (0, \pi)$, implies $\ddot{\psi}_1, \ddot{\psi}_2 \neq 0$. Therefore, the phases start evolving towards $\psi_1 > \psi_2$, i.e., towards a state of different frequencies. The frequency evolution implies a change in charge of the two solitons, since the frequency uniquely parameterizes the family of Q-ball solutions of (in general) different charge. Hence, a non-trivial complex phase evolution ensues due to nonlinear scalar interactions, implying charge transfer between the two Q-balls, and altering the nature of the force (7).

Furthermore, in the presence of gravity (i.e., in the case of BSs), no nonlinear scalar potential is required for non-trivial interactions to occur. In Ref. [38], an effective repulsion was observed in the collision of two mini BSs (stars in linear scalar models) when comparing the case when the complex scalar field is *anti-symmetric* under star interchange, i.e., in (6), if $\alpha = \pi$, $\phi_1 = \phi_2$, and $\omega_1 = \omega_2$, then $\Phi \leftrightarrow -\Phi$ when $\mathbf{x}_1 \leftrightarrow \mathbf{x}_2$, to the symmetric case. Related to this, static spacetimes corresponding to BSs with two (or more) peaks have been constructed in the linear scalar model, which can be thought of as corresponding to two non-spinning BSs kept in equilibrium by the same relative phase difference [77–79]. In the following, we will refer to this equilibrium state as the dipolar BS (DBS) solution.

Lastly, angular momentum, present in rotating Q-balls, spinning BS solutions, or in inspiraling binary BSs, plays an important role in the evolution of the phase, since angular momentum and the appearance of vortices in a massive complex scalar theory are tightly connected. To illustrate this, we restrict to a flat spacetime, where we can use the symmetries of the background to define local notions of angular momentum. We define the angular momentum density ρ_A with respect to the Killing field η_A associated with the rotational symmetry in the A -th direction as $\rho_A = T_{0j} \eta_A^j$, in Cartesian coordinates. From the $U(1)$ complex scalar stress-energy tensor, we know that $T_{0i} = -2\dot{\phi}\partial_i\phi - 2\dot{\psi}\phi^2\partial_i\psi$, when decomposing $\Phi = \phi e^{i\psi}$. Therefore, the vorticity in the A -th direction, which we define as $\nu_A := \eta_A^j \partial_j \psi$, is related to the associated angular momentum density by

$$\rho_A \sim \phi^2 \nu_A \partial_t \psi, \quad (8)$$

where we dropped the ψ -independent term. In the case of rotating Q-balls, with field profile $\psi = \omega t - m\varphi$, we find that the vorticity in all directions, excluding the spin-direction, vanishes. The latter is simply given by $\rho_{\text{spin}} = -2\omega\phi^2\nu_{\text{spin}} = 2m\omega\phi^2$. In the case of the rotating BS, the expression is modified only by curvature corrections. This makes the connection between vorticity and angular momentum manifest, as the total angular momentum in the rotating Q-ball (and BS) solution is quantized by the vortex index m , as $J = mQ$. Note, a vortex in the $U(1)$ nonlinear scalar models considered here does *not*, by itself, contain energy. Hence, vortices can be created and destroyed spontaneously, as long as angular momentum is conserved. This is in stark contrast to, for instance, cosmic strings in global $U(1)$ -Higgs or Higgs-Abelian models, where the string itself is a non-zero energy solution that is topologically protected.

Ultimately, the evolution of the complex phase of the scalar field determines the type of self-interaction-induced momentum and charge transfer between two Q-balls, as well as the angular momentum present in the solution, while these effects are exponentially suppressed by the distance between the solitons.

C. Scalar interactions in a binary BS inspiral

Let us translate the findings discussed in the previous section from the flat spacetime case, to the self-gravitating BS case in the context of a binary inspiral. For most of the early inspiral of a binary BS, the scalar interactions are exponentially suppressed, and hence, subdominant to the gravitational interactions. At this stage of the inspiral, the scalar phase of each star grows linearly according to the star's stationary frequency. In the late inspiral, i.e., when $D \sim 1/k_i$, scalar interactions increase in importance, and the phases of each star start to differ from the stationary prediction, i.e., $\ddot{\psi}_{1,2} \neq 0$. At this stage, linear predictions for the evolution of the scalar phase break down, and nonlinear simulations are necessary. Many of the effects present in Q-balls cannot be easily quantified in the context of dynamical gravity due to a lack of background symmetries and well-defined local quantities. Therefore, in the following we attempt to provide intuition for the scalar interaction-driven physical processes active during the later inspiral and merger of binary BS, and leave a more rigorous and systematic study to the later sections.

In order to understand the phase evolution within a binary BS during the late inspiral, it is instructive to begin by studying the phase of a single, boosted, non-spinning BS with field profile

$$\Phi = \phi(\mathbf{x})e^{i(\omega t + \alpha)} \quad (9)$$

in the stationary frame. With the primed coordinates (t', \mathbf{x}') denoting a boosted frame, defined by the boost vector β^i , the complex phase of the boosted BS in the $t' = 0$ slice is

$$\psi(\mathbf{x}') = \omega \beta^i x'_i + \alpha \mod 2\pi. \quad (10)$$

Therefore, due to the mixing of temporal and spatial degrees of freedom in the Lorentz boost, the complex phase of the scalar field is a monotonic function of *space* in the boosted frame, with slope determined by the star's frequency ω^2 . We now move to the case of an inspiraling binary BS. The construction of binary BS initial data satisfying the Hamiltonian and momentum constraints is outlined in Appendix D, with further details in [80]. Here, we simply note that the binary's scalar field is a superposition of two isolated stars, boosted with velocity v_1, v_2 along β_1^j, β_2^j . Explicitly, the constraint-solving scalar field profile in the initial time-slice in the center of mass frame is

$$\Phi_{\text{BBS}} = \phi_1 e^{i(\omega_1 \beta_1^i x'_i)} + \phi_2 e^{i(\omega_2 \beta_2^i x'_i + \alpha)}. \quad (11)$$

Therefore, in the center of mass frame, the spatial dependence of the complex phase ψ_{BBS} of Φ_{BBS} is

$$\psi_{\text{BBS}} \approx \begin{cases} \omega_1 \beta_1^i x'_i, & \phi_1 \gg \phi_2, \\ \omega_2 \beta_2^i x'_i + \alpha, & \phi_2 \gg \phi_1. \end{cases} \quad (12)$$

In the regions with $\phi_1 \sim \phi_2$, an infinite set of $|q| = 1$ vortices appear. In fact, if the scalar field initial data of the binary BS is constructed by superposing the individual star's fields, then these vortices cannot be removed, unless all angular momentum is removed from the system (e.g., in a head-on collision). We find that a subset of these vortices becomes dynamically important in the binary evolutions discussed in the remainder of this work.

To illustrate this, and the subsequent evolution, we consider a non-spinning binary BS in the repulsive scalar model (5) with coupling $\lambda/\mu^2 = 10^3$. The stars of the binary are prepared with frequencies $\omega_1/\mu = 0.9$ and $\omega_2/\mu = 0.86$ and initial phase-offset $\alpha = 0$. The initial coordinate separation is $D = 20M_0$, with binary ADM mass M_0 (see Table I for details on the parameters of the initial data). In the language of the previous section, this choice enables phase evolution and breathing behavior. We comment on the former below, while the latter is likely a small effect on timescales larger than the orbital timescales of this binary. In Figure 2, we show the magnitude ϕ_{BBS} and phase ψ_{BBS} of the equatorial plane of the binary BS at four different times throughout the evolution. We focus first on the initial time-slice. The less compact of the two stars, i.e., the star with smaller central scalar field magnitude, is the star with smaller charge and larger frequency, $\omega_1/\mu = 0.9$. The complex phase of this binary, shown in the bottom row of Figure 2, illustrates the structure discussed above. The phase is a monotonically increasing function of space in the boost direction on either side of the black dashed line, indicating where $\phi_1 \sim \phi_2$. The slope of the phase is different on either side of $\phi_1 \sim \phi_2$ in the equatorial plane, since $\omega_1 \neq \omega_2$. The surface of $\phi_1 \sim \phi_2$ is a 2-dimensional surface in the spatial hypersurface separating regions of $\phi_2 > \phi_1$ from those with $\phi_2 < \phi_1$. Lastly, in the equatorial plane, along the line of $\phi_1 \sim \phi_2$ there is a set of

Frequency	C	x_0/M_0	v_x	J_0/M_0^2	α	e
$\omega_1/\mu = 0.90$	0.08	-10.69	0.12	0.9	0	0.13
$\omega_2/\mu = 0.86$	0.12	9.31	-0.10			

Table I. The properties of the non-spinning binary BS initial data discussed in the main text. The two stars have frequencies $\omega_{1,2}$, with initial phase offset α , are positioned at coordinate locations x_0 and $y_0/M_0 = 0$, have boost velocities v_x and $v_y = 0$ (with Newtonian eccentricity e), compactness C , and mass-ratio $\tilde{q} = 1.13$. Here M_0 is the ADM mass, and J_0 is the similarly defined global angular momentum, the latter given by eq. (7.63) of Ref. [81]. Note, this definition of angular momentum, albeit commonly used, is not free from gauge-dependency (for further details, see Ref. [81]).

² The magnitude ϕ is simply Lorentz contracted in the boost direction.

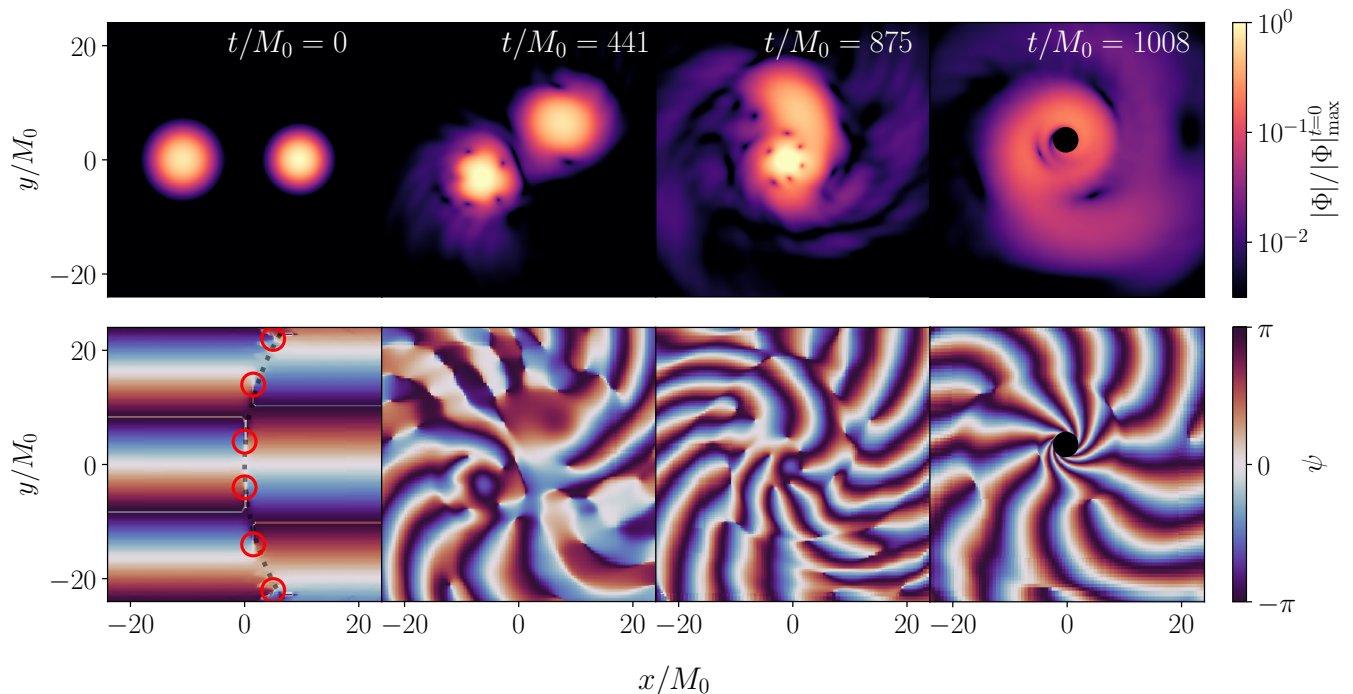


Figure 2. We show four snapshots of the equatorial plane during the merger of a non-spinning binary BS with frequencies $\omega_1/\mu = 0.9$ and $\omega_2/\mu = 0.86$, with no initial phase-offset $\alpha = 0$, total ADM mass M_0 , an initial coordinate separation $D = 20M_0$, and in the repulsive scalar model (5) with $\lambda/\mu^2 = 10^3$. The compactness of the higher and lower frequency star is $C = 0.08$ and $C = 0.12$, respectively. The total angular momentum points into the page, and the orbit has Newtonian eccentricity $e = 0.13$. The final black hole parameters are shown in Figure 3. (*top row*) We show the magnitude of the scalar field $|\Phi|$, normalized by the maximum magnitude of the scalar field in the initial time-slice $|\Phi|_{\max}^{t=0}$. (*bottom row*) We show the complex phase $\psi \in (-\pi, \pi)$ at the corresponding times in the equatorial plane. At $t/M_0 = 0$, we indicate the locations of the $q = 1$ vortices by red circles, while we indicate the surface of $\phi_1 \sim \phi_2$ defined below (12) with a black dashed line. Notice, the white lines in the first panel of the bottom row are interpolation artifacts and correspond to $\psi = \pm\pi$.

$q = 1$ vortices indicated with red circles.

The chosen boost parameters do not lead to a quasi-circular inspiral, but rather to an orbit with non-zero eccentricity. Therefore, the stars go through an initial orbital phase, during which their (coordinate) distance increases over time. During this time, the scalar interactions are exponentially suppressed, and the dynamics are largely dominated by gravitational interactions of the stars. Throughout this phase, the complex phase of each star increases approximately linearly, and independently, in time. After passing the apoapsis, the coordinate distance between the stars decreases, leading to enhanced scalar interactions. The closest approach is achieved around $t/M_0 = 350$. During the periapsis passage, there is significant overlap between the two scalar field profiles. The evolution of ψ is no longer approximately linear in time. The enhanced scalar interaction, in conjunction with the presence of the vortices in ψ between the two stars, leads to the transfer of these vortices onto *both* of the BSs. In the second snapshot of Figure 2, the vortices can be seen just after the closest approach. After the periapsis, the vortices orbit around each individual star in the same direction as the overall orbital motion. Qualitatively, the orbiting vortices indicate angular momentum

transfer from the orbit to the spin angular momentum that can be assigned to each star. While stationary BSs cannot rotate perturbatively [51], time-dependent solutions may. During the second close encounter, the scalar interactions dominate the dynamics. The star with the larger frequency transfers large amounts of scalar charge onto its heavier companion. This process is shown in the third snapshot of Figure 2. As the heavier star accretes scalar matter, its charge and central scalar field magnitude increase. Ultimately, the lighter (and less compact) star is completely tidally disrupted and accretes rapidly onto the heavier companion. The mass of this companion increases beyond the maximum mass the star can stably support, and it collapses into a black hole. This situation is shown in the fourth panel of Figure 2. The remnant black hole moves through the surrounding residual scalar matter, continuing to accrete it.

The gravitational radiation, as well as the final black hole parameters, are shown in Figure 3. There, we also compare to an evolution of the same binary BS initial data, except with initial phase-offset of $\alpha = \pi$. This case has two important features that distinguish it from the $\alpha = 0$ case: (*i*) The $\alpha = \pi$ case collapses to a black hole roughly $200M_0$ earlier than the $\alpha = 0$ case, and

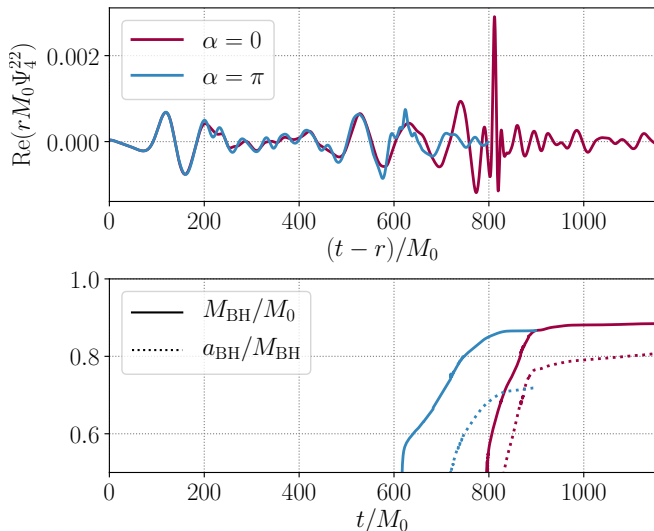


Figure 3. (*top panel*) We show the $(\ell, m) = (2, 2)$ mode of the $s = -2$ -weighted spherical harmonic components of the Weyl Newman-Penrose scalar Ψ_4 (extracted at coordinate radius $r = 100M_0$) emitted during the binary BS inspiral of the case with initial phase-offset $\alpha = 0$ shown in Figure 2 and discussed in the main text. We compare this to the GWs from the same binary inspiral with initial phase-offset $\alpha = \pi$. (*bottom panel*) The mass M_{BH} (solid) and dimensionless spin parameter a_{BH} (dashed) measured from the apparent horizons of the remnant black holes formed in the inspiral of the top panel. We evolve the $\alpha = \pi$ case for only roughly $900M_0$.

(ii) the gravitational waveforms differ in amplitude from $t = 200M_0$ to $t = 500M_0$. The high-frequency features in the waveform shown in the top panel of Figure 3 originate from time-dependent features on scales smaller than the sizes of the stars. Comparing the orbital period of the vortices around the center of each star with the frequency of the small scale features in the emitted GWs, we can identify the orbiting vortices as the source of the high-frequency GWs. The differing amplitudes indicate that the vortices in the $\alpha = \pi$ case are surrounded by larger $|\Phi|$ values. Consulting (8), this implies also a locally enhanced angular momentum density. This is consistent with finding (i). Larger angular momentum transfer from the orbit to the spin implies earlier merger times, and hence, a more rapid transfer of charge to the heavy star and subsequent black hole formation. The final black hole parameters are, however, roughly independent of the initial phase offset. In fact, the spin angular momentum of the remnant black hole is comparable to that formed by the merger of a binary neutron star or binary black hole. Hence, beside the residual scalar matter, the remnant black hole retains little memory of the type of binary it was made from.

A few remarks are in order. Many of the statements above are purely qualitative in nature, and are mainly made to provide intuition. In particular, the transfer of orbital to spin angular momentum deserves a more

rigorous analysis (e.g., using techniques developed in Refs. [82, 83]). The evolution of the scalar phase during the second encounter is nonlinear, making it challenging to gain intuition from applying linear methods discussed in the previous section. In the following section, we return to the dependence of the GWs on the initial phase and a more systematic analysis of the phase evolution. Furthermore, the use of vortices as a tool to understand the nonlinear phase evolution and to predict the remnant is the subject of Secs. II E and III.

D. Gravitational wave imprints

In the previous two sections, we first reviewed the importance of the scalar phase evolution for the nonlinear dynamics of scalar solitons in the absence of gravity, and then qualitatively applied some of these concepts to the case of an inspiraling non-spinning binary BS. In this section, we investigate the role of the scalar phase in the inspiral and merger of a non-spinning binary BS and the emitted GWs more systematically. The variation of the scalar phase in binary BS mergers has been studied only in the case of head-on collisions in Refs. [8, 33, 38, 42, 84] (see Ref. [47] for a study in the PS case). Here, we consider the impact of the scalar interactions on the *inspiral* of a binary BS and connect our observations directly to the physical intuition provided in Sec. II B, for the first time. We find several significant differences between the head-on collisions studied in [8, 33, 38, 42, 84] and the inspirals considered here: (i) the effect of the scalar interactions accumulate secularly throughout the inspiral, eventually resulting in strong de-phasing and modulations of the emitted GW amplitudes; (ii) vortices appear due to the orbital angular momentum and drive dominant high-frequency features in the emitted GWs at late times during the merger; and (iii) the time to collapse to a black hole post-merger depends sensitively on the scalar interactions, while the remnant's properties are mostly insensitive to the scalar interactions driving the proceeding dynamics.

In order to illustrate the role of the scalar phase and vortex structure during the inspiral, merger, and ring-down, we consider a non-spinning binary BS in the repulsive scalar model given by (5) with $\lambda/\mu^2 = 10^3$, and focus on an equal frequency case with $\omega_1 = \omega_2 = 0.9\mu$. With a compactness of $C = 0.08$ for each star, the impact of the scalar interactions is enhanced compared with a system consisting of highly compact constituent BSs (and $\omega \ll \mu$), since at fixed separation of the stars' center of mass, the overlap of the two stars' scalar fields is larger. The constraint satisfying initial data is constructed using the methods outlined in Appendix D. In the initial time slice, the binary system has ADM mass M_0 , the stars' coordinate positions are at $x_0/M_0 = \pm 10$ and $y_0/M_0 = 0$ (hence, initial coordinate separation $D = 20M_0$), and the initial coordinate velocities are $v_x = 0$ and $v_y = \mp 0.12$ (with these parameters the New-

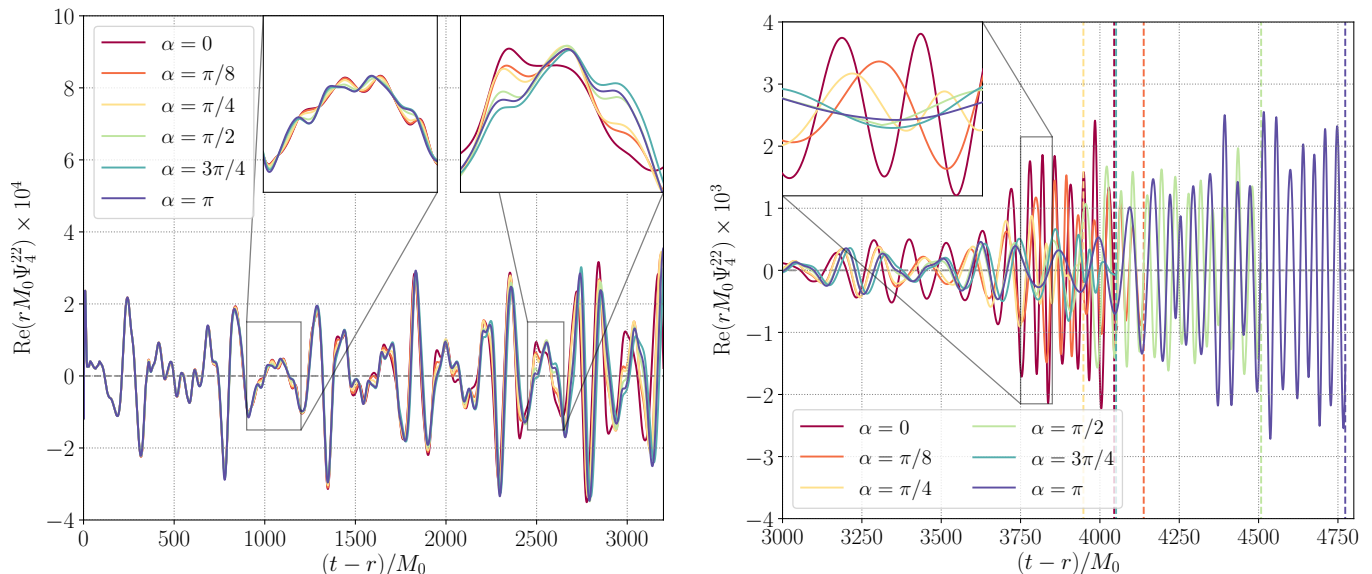


Figure 4. The GWs (extracted at a coordinate radius $r/M_0 = 100$) during the inspiral (*left*) and merger (*right*) of the binary BS described in the main text. The different cases correspond to identical initial binary systems, except with different values of the phase offset α in the range 0 to π . Specifically, we show the $(\ell, m) = (2, 2)$ $s = -2$ -weighted spherical harmonic component of the Newman-Penrose scalar Ψ_4 as a function of retarded time $t - r$. The differences between the various α -cases are due to the enhancement of nonlinear scalar effects during each close encounter of the binary and towards merger, as the separation between the stars shrinks. Notice the different scale used on the left and the right. After merger, the waveforms are terminated around the time when the system collapses to a black hole, which is indicated by a vertical dashed line. We show the GWs after gravitational collapse of the $\alpha = 0$ and π cases in Figure 5.

tonian eccentricity is $e = 0.15$). These initial velocities were chosen to result in an eccentric orbit, with multiple periaapses before final merger. This allows us to observe the effects of repeatedly enhanced and suppressed scalar self-interactions on the GWs. In order to study the impact of the scalar field phase on the inspiral, we vary the initial phase-offset α between the BSs considering the values $\alpha \in \{0, \pi/8, \pi/4, \pi/2, 3\pi/4, \pi\}$. Note that in this strong-coupling regime of the repulsive scalar model, stable rotating $m = 1$ BSs were demonstrated to exist in Ref. [57] (and in Newtonian gravity in Ref. [58]). However, we choose binary BS parameters that are expected to result in the formation of a rotating black hole since the sum of the charges of the constituent stars is larger than the maximum charge of *both* the $m = 0$ and $m = 1$ families of solutions, and indeed we find collapse post-merger.

In Figure 4, we show the GWs emitted during the inspiral of this binary BS for each initial phase offset α . Focusing first on the $\alpha = 0$ case, the non-negligible eccentricity in the binary is reflected in the gravitational waveform as periodic peaks around $(t - r)/M_0 \approx 250, 750, 1300, 1800, 2300$, and 2750 , corresponding to the close encounters of the stars. In between these close encounters, the GW signal is characterized by a high-frequency component emerging from spurious oscillation modes excited in the individual stars due to the way the initial data is constructed. (Though we do not do so here, these spurious oscillations can be alleviated by modifying

the superposition of the two isolated boosted stars and utilizing a different scaling for the conformal kinetic energy of the scalar field, as shown in Ref. [80].) Though the cases with different values of α initially have essentially indistinguishable orbits and GWs, following the first encounter around $(t - r)/M_0 \approx 250$, the differences in the GW amplitude $|\Psi_4^{22}|$ grow³ (see also the two insets). During the periods of large separation between the stars, the scalar phase of each star evolves approximately linearly in time. However, scalar interactions are exponentially enhanced during each close encounter, and become more significant as the orbital period and periaapse distance shrink due to GW emission during the course of the merger. Since the nonlinear interactions depend on, and affect the scalar phase of the star, as discussed in Sec. II B, they secularly affect the evolution and GWs of the binary BS system.

These differences in Figure 4 are primarily differences in the GW amplitude. However, as can already be seen

³ All cases considered here were obtained with identical numerical setups both to construct the initial data and to evolve it, suggesting that the *relative* differences in the GWs of the evolutions shown in Figure 4 are driven by scalar interactions, rather than being due solely to numerical truncation error. However, as discussed in Appendix D, the estimated truncation error in the GW amplitude is comparable to the difference between the cases with different values of α .

there, at late times, there is also a non-negligible *dephasing* between the waveforms. This can be clearly seen in Figure 4, where we show the GWs emitted during the late inspiral and merger of the binary systems. Though the exact point of contact for the two stars is not well-defined, As the stars begin to merge, the GW amplitude increases significantly—by up to an order of magnitude—as can be seen comparing the left and right panels of Figure 4 (note the difference in scales). While the exact point of contact for the two stars is not well-defined, one can loosely determine the merger time by this sudden increase in amplitude. It is clear from the right panel of Figure 4 that this time depends strongly on the initial phase offset α . For instance, the $\alpha = 0$ case merges around $(t - r)/M_0 \approx 3750$, while the binary with initial phase offset $\alpha = \pi$ merges at $(t - r)/M_0 \approx 4150$. After the merger, the system enters into a transient state consisting of a dynamical remnant star that is temporarily prevented from collapsing due to excess energy and/or angular momentum, analogous to what may happen post-merger in a binary neutron star. A series of scalar vortices (some of which still present from the initial data) rapidly orbit around the center of mass of the remnant indicating large perturbative angular momentum of the *hypermassive BS*.⁴ These vortices are small scale features orbiting on the scale of the original constituent stars, which lead to high-frequency GW emission (similar to what we described in Sec. II C). This is reflected in the sudden increase in the GW frequency after the merger of the stars, as shown in Figure 4, which matches the orbital frequency of the vortices around the center of mass of the hypermassive BS. The length of this hypermassive state depends on the initial phase-offset, and hence, on the nonlinear scalar dynamics. For instance, the hypermassive phase in the $\alpha = \pi/4$ case only lasts $t/M_0 \approx 150$, while for the $\alpha = \pi$ case, it lasts $t/M_0 \approx 600$. The latter is longer lived, since the symmetry gives rise to a vortex at the center of mass throughout the evolution, which acts to delay the gravitational collapse of the hypermassive remnant. However, in all the cases with different values of α , we find eventual collapse to a black hole, at times indicated by the vertical dashed lines in Figure 4. We cannot identify a clear trend in the dependence of the collapse time on initial scalar phase offset α . This may be explained by the fact that the intrinsic BS inverse frequency $\omega_{1,2}^{-1} \approx 1.4M_0$ is much shorter than the time to merger $T_m \sim \mathcal{O}(10^3 M_0)$, so that the repeated scalar interactions, operating on timescales $\sim 1/\omega$, accumulate differences nonlinearly throughout the inspiral of length T_m , leading to a significantly different states

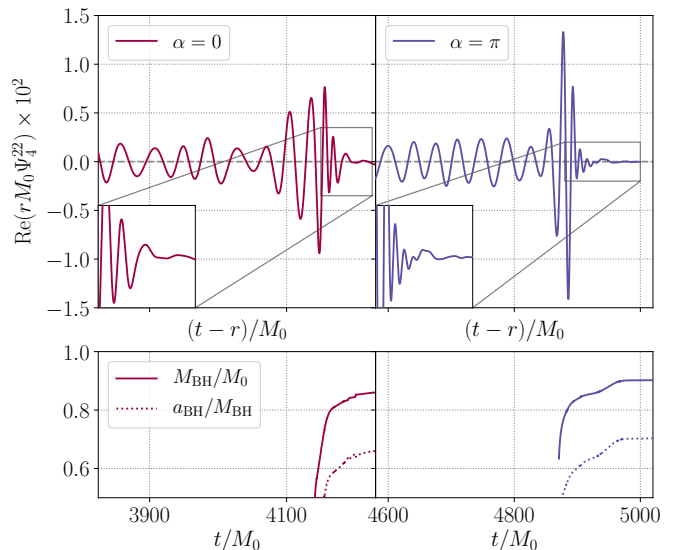


Figure 5. (*top panels*) We show the GWs emitted around the time of black hole formation by the binary BS systems discussed in the main text and shown in Figure 4, for initial phase offsets $\alpha = 0$ and π . Notice the difference in scale compared with Figure 4. (*bottom panels*) The mass M_{BH} and spin parameter a_{BH} of the remnant black holes formed as functions of *coordinate time* t (corresponding to the retarded time $t - r$ in the top panels).

entering the hypermassive phase and subsequent gravitational collapse. Hence, any consistent α -trend present at early times appears lost in the accumulated nonlinear shift.

In Figure 5, we show the GWs through the collapse of the hypermassive BS state to the final remnant black hole in the case of $\alpha = 0$ and $\alpha = \pi$. As pointed out above, the time of collapse is significantly different due to the accumulated nonlinear scalar (and gravitational) interactions. However, the GWs radiated during the collapse to a black hole are qualitatively similar. The amplitude rapidly increases by a factor of a few and then decays. This sudden increase in amplitude is likely driven by the vortices in the hypermassive remnant being forced onto tighter orbits with higher orbital frequency just before horizon appearance. The subsequent ringdown differs somewhat from a spinning black hole in vacuum due to the residual scalar matter (of mass $\sim 0.1M_{\text{BH}}$) orbiting the black hole. As can be seen in the insets in the top panel of Figure 5, this has the effect of washing out the exponential decay of the GW amplitude. The mass and dimensionless spin parameters of the remnant black hole are only slightly smaller, in the $\alpha = 0$ case compared to the $\alpha = \pi$ case. Therefore, despite the quantitatively different inspiral and merger dynamics, depending sensitively on the initial scalar phase configuration of the stars, the remnant black holes show only little memory of the initial BS binary from which they emerged. In fact, the dimensionless spin of the remnant black holes

⁴ In analogy with the neutron star case (see, e.g., Ref. [85]), here we use hypermassive to refer to an object with total mass above the maximum stable $m = 1$ rotating BS within the same scalar model. We use hypermassive BS to refer to the merger remnants even when these are highly perturbed, and far from equilibrium solutions.

are roughly $a_{\text{BH}}/M_{\text{BH}} \approx 0.7$, which is consistent with the quasi-circular merger of a non-spinning equal-mass binary black hole, and the lower range of the values of $a_{\text{BH}}/M_{\text{BH}} \approx 0.7\text{--}0.8$ found for prompt collapse following a binary neutron star merger (see, e.g., Ref. [86, 87]).

In summary, we find that, during the late inspiral of a binary BS, scalar interactions, which depend on the scalar phase offset between the stars, have a significant, cumulative effect, resulting in modulations of the amplitude and de-phasing of the GWs, and affecting the merger time by hundreds of light crossing times of the system. The two stars merge into a hypermassive BS remnant that is characterized by a series of vortices orbiting rapidly around its center of mass, resulting in emitted high frequency GWs. Lastly, the hypermassive remnant collapses to a remnant black hole with mass and spin which, despite the large difference in the inspiral dynamics, we find to be largely insensitive to the nonlinear scalar dynamics prior to collapse.

Here, we considered the special case of an equal frequency binary BS. Therefore, the scalar interactions in the initial binary BS are completely characterized by the scalar phase offset α between the stars. In a more complex scenario with $\omega_1 \neq \omega_2$, the different linear evolutions of both stars' phases would lead to oscillations in the nature of the scalar interactions at characteristic frequencies $\omega_1 \pm \omega_2$. The oscillatory nature of the interaction accumulates nonlinearly during the later inspiral, with the phase offset it leads to at the point of contact depending on the length of the inspiral. The value of this phase offset just before merger will likely have a strong effect on the qualitative behavior of the system after merger (when nonlinear interactions drive the dynamics), as it does in the scenario studied here. In fact, in Refs. [47, 84], it was noted that in the case of head-on collisions, the GW emission is predictably dependent on the phase-offset at early times and the point of contact. Our results, however, suggest that in the case of a BS inspiral, the nonlinear interactions prior to merger, which accumulate secularly, render a reliable prediction of the phase-offset at the point of contact challenging.

E. Remnant map

In the previous section, we demonstrated the complex dependence of the scalar and gravitational dynamics during the merger process on the binary BS parameters, in particular the scalar phase of the BSs. In order to provide a more straightforward understanding of these systems, here we outline and motivate a small set of criteria, and an associated mapping, in order to guide predicting the outcome of a given merger of a binary BS, i.e., to determine whether a spinning BS, non-spinning BS, or a black hole will be formed.

1. Details of the remnant map

Recall, within a given scalar (or vector) model, there exists a set of one-parameter families of BS (or PS) solutions \mathbb{B}_m indexed by the azimuthal index m (excluding “excited” states with a higher number of radial nodes). A representative $\mathcal{B} \in \mathbb{B}_m$ of the one-parameter family of star solutions (for fixed m) is identified, in general, by its mass M , charge Q , frequency ω , and angular momentum J ($J = 0$ for spherical stars). Crucially however, if one restricts to the *stable* branches of a family of solutions, a particular BS (or PS) solution is *uniquely* identified by the charge alone $\mathcal{B}(Q)$.

During a binary BS (or PS) merger, energy and angular momentum will come both from the constituent stars, as well as from the orbit, and some fraction of these quantities will be carried away both by gravitational and scalar radiation. The total boson number (i.e., the $U(1)$ -charge of the system), on the other hand, will only be affected by scalar radiation. We expect this to be subdominant to gravitational radiation since the scalar field is massive, and higher energy processes are required to elevate a bound boson into an asymptotically free state. Therefore we will make the approximation that the scalar charge is conserved during the merger here, but return to the implications of scalar particle loss below. Hence, a core assumption of the mapping from the binary's constituent BSs (formally, $\mathcal{B}_1 \in \mathbb{B}_{m_1}$ and $\mathcal{B}_2 \in \mathbb{B}_{m_2}$) with charges $Q_{1,2}$ into the remnant solution \mathcal{B}_r of charge Q_r is charge conservation $Q_1 + Q_2 = Q_r$.

Combining the assumption of charge conservation, as well as restricting to the stable branches of the one-parameter families of solutions $\mathbb{B}_{m_{1,2}}$, enables us to introduce \mathcal{R}_F , which maps all properties of the merging binary BS (or PS), i.e., properties of $(\mathcal{B}_1, \mathcal{B}_2)$ into those of the remnant \mathcal{B}_r , formally written as

$$\mathcal{R}_F(\mathcal{B}_1, \mathcal{B}_2) = \mathcal{B}_r. \quad (13)$$

Since $\mathcal{B}_{1,2}$ are uniquely identified by any pair of the constituents properties (e.g., the frequencies $\omega_{1,2}$), the map \mathcal{R}_F can take various explicit forms. For example, the explicit map of the frequencies of the inspiraling binary (ω_1, ω_2) into the frequency of the remnant ω_r is $\mathcal{R}_F^\omega(\omega_1, \omega_2) = Q_r^{-1}[Q_1(\omega_1) + Q_2(\omega_2)] = \omega_r$, using charge conservation and the inverse Q_r^{-1} of $Q_r(\omega_r)$ for a chosen family of solutions.

So far, we have not specified into which family of stationary solutions $\mathcal{B}_r \in F$ the remnant map \mathcal{R}_F maps (this freedom is indicated by the subscript of \mathcal{R}_F). In principle, F could be *any* set of stationary solutions allowed in the scalar (or vector) theory at hand, i.e., (3) and (C1), that satisfies the charge conservation assumption; for instance, a non-rotating BS, a DBS solution, a spinning BSs, etc. However, many of these possibilities can be rejected using a series of conditions which the remnant has to approximately satisfy. Of course, it is possible that are no suitable remnant star solutions for a given binary. For example, the total charge of the binary

may be above the maximum charge of any remnant non-vacuum family, $Q_1 + Q_2 > Q_r^{\max}$, in which case one may expect a black hole to form. As we show below, the combination of these conditions and the remnant map (13) can be used to understand the outcome of even complex merger scenarios. In the following, we introduce the conditions first, and then return to a practical application of the formal map (13).

The first set of conditions, we call the *kinematic conditions*. The masses and angular momentum of the constituents of the binary, as well as the remaining orbital angular momentum at merger J_{orb} , should satisfy

$$\begin{aligned} 1. \quad M_1 + M_2 &\gtrsim M_r, \\ 2. \quad J_1 + J_2 + J_{\text{orb}} &\gtrsim J_r, \end{aligned} \quad (14)$$

at the point of contact of the stars. Here, M_r and J_r are the remnant solution's total mass and angular momentum. This condition holds only for aligned-spin scenarios and here we are neglecting the correction from the orbital energy as being small.

Secondly, the *stability condition*, states that the remnant stationary solution must be free of any linear or nonlinear instability:

$$3. \quad \mathcal{B}_r \text{ is stable.} \quad (15)$$

Lastly, the *vortex condition* concerns the scalar phase dynamics. We conjecture that the vortex number m_r of the final remnant of the binary merger is given by the vortex number of a closed loop Γ enclosing the center of mass at the point of contact of the stars as well as all significant vortex lines of the merging binary:

$$4. \quad m_r = \frac{1}{2\pi} \oint_{\Gamma} d\ell_i D^i \psi. \quad (16)$$

By significant vortex lines, we mean to exclude, for example, those that may arise as perturbations to the constituent BSs during the inspiral (as in Fig. 2), though we will return to this below. Here, Γ is negatively oriented with respect to the total angular momentum⁵ J_{ADM}^μ . These conditions are approximate, and we explicitly show below the degree to which they must be satisfied in example mergers.

The procedure to determine the family of stationary solutions F and identify the remnant \mathcal{B}_r is as follows: (i) Construct \mathcal{R}_F for a plausible family of remnants F , (ii) reject this mapping if it violates one of the four conditions listed above, and (iii) begin at step (i) with a different plausible family. Therefore, the map (13) is used to eliminate possibilities until the correct remnant remains. A priori, considering all plausible families F appears to be a daunting task. However, in practice, we find that only

focusing on the families of non-spinning and $m = 1$ rotating isolated stars (within the considered model) suffices, with the vortex condition (16) efficiently discriminating between the two. For example, a DBS solution can be approximated by the sum of two non-spinning stars, particularly in the Newtonian limit (see Ref. [79]).

In Ref. [44], a similar set of criteria was considered (in particular conditions 1.–3.). However, crucially, here we add the vortex condition (16), and point out its vital role in the binary merger process below. Furthermore, while the “point of contact” is an ill-defined notion in the case of BSs (and PSs), the more relativistic the stars become, the easier it becomes to identify the point of contact. Similarly, the vortex condition should be regarded somewhat approximately, as we will show using examples of un-equal mass mergers of a rotating and a non-rotating BS. In the special case of a head-on collision (i.e., with exactly vanishing angular momentum), no vortex exists. Lastly, this map may be extended to PSs as well by the addition of another condition, which governs the relative *direction* of the vector fields of a given PS binary. We return to applying this remnant map to PS in Sec. III A, but leave a more detailed analysis to future work.

2. Applying the remnant map

We now illustrate the importance and utility of the above considerations with an example, in particular, of a binary BS where a single remnant is not formed at merger. We consider a spinning binary BS inspiral of identical $m_1 = m_2 = 1$ BSs with $\omega_1 = \omega_2 = 0.4\mu$ in the solitonic scalar model with $\sigma = 0.05$ [see (4)], of compactness $C = 0.12$, at an initial coordinate distance of $D = 10M_0$ and initial phase-offset of $\alpha = 0$. The orbit of the binary is set up such that $|J_{\text{orb}}| < |J_1 + J_2|$, with J_{orb} anti-aligned with J_1 and J_2 . Lastly, we note that, if the spinning binary BS initial data is prepared with a vanishing phase-offset initially, the symmetry of the binary fixes the location of a $q = -1$ vortex at the center of mass of the system throughout the inspiral. Notice that each *individual* spinning star has vortex number $m_{1,2} = 1$ (with respect to the total angular momentum).

We can now employ the remnant map (13), and consider possible outcomes of this inspiral. First, because of the vortex condition (16) with $m_r = q + m_1 + m_2 = 1$, no single non-spinning star can be formed, as that would require $m_r = 0$. Secondly, the total angular momentum of the inspiraling system, $J_{\text{total}} = J_1 + J_2 + J_{\text{orb}}$, is *smaller* than the angular momentum of a remnant spinning BS in the $|m_r| = 1$ family of solutions, as can be checked explicitly using (13). Therefore, using the remnant map with (16) and conditions (14), we can already rule out that the remnant \mathcal{B}_r is a single non-spinning BS or a $m_r \geq 1$ rotating BS [$|m_r| > 1$ would violate both the vortex condition and, likely, the stability condition (15)]. Hence, if the merger does not result in a black hole, the only option is that the remnant consists of at least *two* stars. The

⁵ Note, paired with the choice of $J \rightarrow -J$ and $m \rightarrow -m$ (or $Q \rightarrow -Q$), the negative orientation of Γ with respect to the total angular momentum of the remnant is a convention.

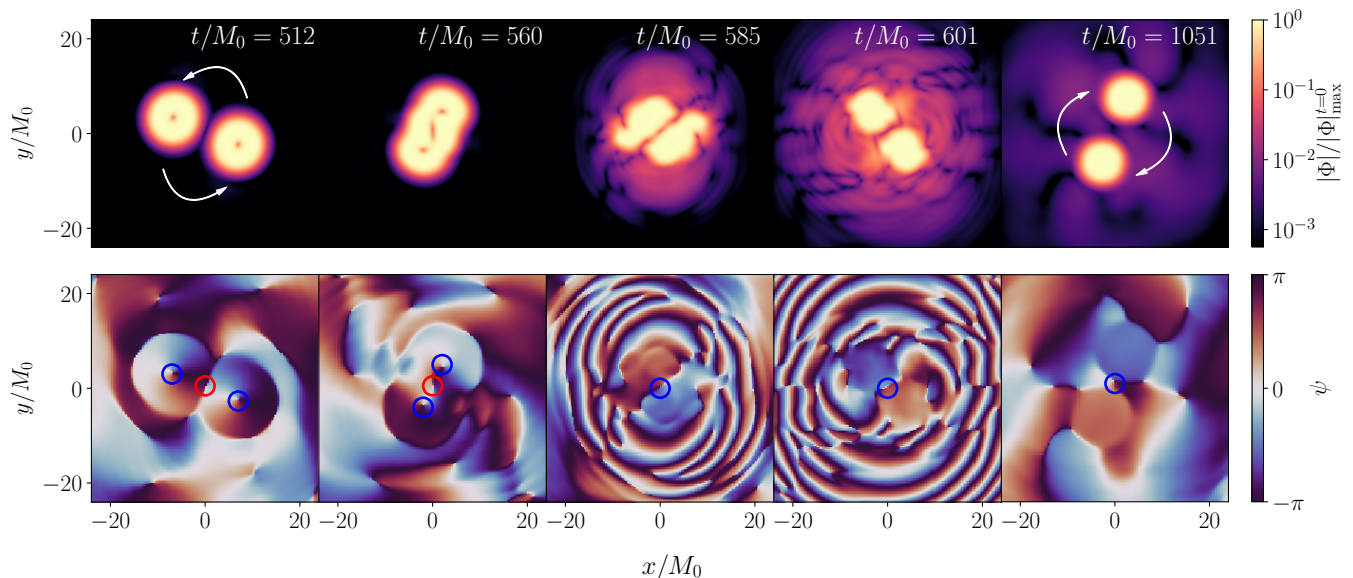


Figure 6. Five snapshots of the equatorial plane of the spinning binary BS inspiral discussed in Sec. II E. (*top row*) We show the magnitude of the scalar field in the equatorial plane, normalized by the initial maximum of the magnitude $|\Phi|_{\max}^{t=0}$. (*bottom row*) We present the corresponding scalar phase $\psi \in (-\pi, \pi)$. We indicate the location of all relevant $q = -1$ vortices by red circles, and all relevant $q = 1$ vortices by blue circles. (All vortex indices are measured with respect to the total angular momentum). The arrows indicate the direction of rotation of the inspiraling binary and the binary endstate.

reflection symmetry of the system with respect to the center of mass (due to the choice of identical stars with vanishing phase-offset in the initial data) suggests that the remnant is made up of an integer number of identical stars. Furthermore, as we show in Appendix A, a single isolated non-spinning BS is energetically favorable to a $m = 1$ spinning BS of the same charge. Therefore, two non-spinning remnant BSs are energetically favored over two spinning BSs. Finally, due to the $m_r = 1$ vortex of the remnant, the scalar phases of each non-spinning stars will be exactly out of phase with respect to each other. This implies they will be “bouncing” off each other due to the effective repulsion associated with this phase difference reviewed in Sec. II B, analogous to the state found in [38, 77]. Lastly, the two stars (in a configuration similar to the DBS solution) will move around the common center of mass (and the $m_r = 1$ vortex) now with orbital angular momentum J_{total} , i.e., they orbit in the *opposite* direction to the inspiraling orbit. Hence, using (13) we obtain a final state for the system that satisfies all of the above conditions. Therefore, using the remnant map (13) and the four conditions listed above, we were able to qualitatively predict large portions of the *nonlinear* dynamics of the binary system as well as the final remnant and its properties. Of course, we cannot rule out that the final state is composed of more than two stars, which, however, could be addressed in principle by considering, whether four stars as the remnant \mathcal{B}_r is favored over two stars.

We confirm this picture by numerically evolving this spinning binary BS system, as shown in Figure 6. Before entering the regime of strong scalar interactions, i.e., for

times $t/M_0 < 500$, the phases of each spinning star oscillate around the respective central vortex (marked in blue) roughly at the star’s internal frequency. Notably, a $q = -1$ vortex is present at the center of mass by construction of the binary initial data (marked in red). From $t/M_0 \approx 550$ to $t/M_0 \approx 650$, the two stars interact nonlinearly, both gravitationally and through the scalar self-interaction. During this interaction, the two $m_{1,2} = 1$ vortices of the two spinning stars merge with the $q = -1$ vortex of the orbital angular momentum at the center of mass to form a single $m_r = q + m_1 + m_2 = 1$ remnant vortex fixed at the center of mass. Furthermore, the nonlinear interaction of the two spinning stars result in the formation of *two* (approximately) non-spinning BSs. This addition of vortex numbers can equivalently be understood using angular momentum conservation discussed in Sec. II B: The spin angular momenta of the two merging stars add to the *oppositely oriented* orbital angular momentum during the merger. The remnant stars are void of spin-angular momentum, such that the remaining vortex m_r must align with the total (and now only orbital) angular momentum. Finally, the $m_r = 1$ vortex at the center of mass remains and dictates that the two remnant stars are precisely out of phase. The latter can be seen in the last three snapshots of Figure 6. The outcome of the merger is a DBS solution [38, 77], however, with non-zero orbital angular momentum (implying the presence of the central $m_r = 1$ vortex). Hence, we find that this DBS state orbits around the central vortex with the remaining angular momentum (the arrows in Figure 6 indicating the sense of rotation about the center of mass). It is plausible that the final stationary state is

a DBS solution with vanishing angular momentum (i.e., the system radiates the appropriate amount of energy and angular momentum to migrate towards a stationary DBS solution).

This explicitly demonstrates both the utility of the remnant map together with the kinematic, stability, and vortex conditions in predicting the outcome of highly nonlinear mergers, as well as the important role the scalar interactions, in particular, the scalar phase evolution and vortex structures, play during the merger of binary BSs.

III. FORMATION OF ROTATING BOSON STARS

Finding a scenario where a rotating BS forms dynamically from the merger of two non-rotating stars has been an open problem. In the past, numerous attempts and configurations were considered to form a rotating BS remnant from a binary inspiral, most notably in Refs. [43, 44] (see also Refs. [40, 42, 48]). Here, we argue, that all of these attempts violate one or several of the conditions needed to form rotating BSs outlined in the previous section. In particular, we point out that the scalar phase and vortex structure play a pivotal role in forming a persistent rotating BS remnant.

To show this explicitly, we proceed by applying the remnant map and set of conditions from the previous section to this formation scenario in Sec. III A, and demonstrate by numerical evolutions in Sec. III B that some appropriately chosen initial data satisfying these conditions do in fact lead to a rotating remnant. Hence, for the first time, we find rotating BS remnants that form dynamically from the merger of two non-spinning BSs. We then study the robustness of this formation mechanism to variations in angular momentum and scalar phase in Sec. III C, discuss the implications of these conditions on the characteristics of this new formation channel in Sec. III D, and finally, in Sec. III E analyze the merger remnant of a binary where one BS is spinning and the other is non-spinning, showing that whether it is rotating or non-rotating depends on the binary's mass-ratio.

A. Formation criteria & parameter space

We begin by considering how the remnant map (13) relates two non-spinning BS solution to a $m = 1$ rotating BS solution, and in what range the kinematic and stability conditions, defined in (14) and (15) (discussed in Sec. II E), respectively, will be satisfied. We return to a discussion of the vortex condition below. To that end, we consider three different families of non-rotating stars: (i) a repulsive family of BSs with $\lambda/\mu^2 = 10^3$, (ii) a solitonic set of BSs with coupling $\sigma = 0.05$, and (iii) a family of non-rotating PSs (without vector self-interactions). For each of these families of solutions, a corresponding family of $m = 1$ rotating stars exists. We label the fre-

quencies of the constituents of the initial non-spinning binary by ω_1 and ω_2 and choose, without loss of generality, that $\omega_2 \geq \omega_1$. For each combination of stationary stars (ω_1, ω_2) we use the charge conservation mapping (13) combined with the one-to-one charge-frequency relation, $Q_r(\omega_r) \rightarrow Q_{m=1}(\omega_{\text{rot}})$ for corresponding $m = 1$ family of rotating BSs (and PSs) in each of the three considered models to map all properties of the two stars in the initial binary system into the properties of a single *potential* $m = 1$ rotating remnant star.

In Figure 7, we show the results of the above constructed mapping for all three theories. Using this, we are able to apply the kinematic conditions to isolate the parts of the initial non-spinning binary parameter space that are suitable for the formation of a rotating remnant BS. First, we consider condition 1. in (14) (the kinematic condition). In order for the formation of a rotating remnant to be energetically favorable from a non-spinning binary, we must require

$$\mathcal{M} = \frac{M_1 + M_2 - M_{\text{rot}}}{M_1 + M_2} > 0. \quad (17)$$

Here M_1 , M_2 , and M_{rot} are the ADM masses of the stationary isolated non-spinning stars and the rotating star, respectively. From Figure 7, we can deduce that for models (i) and (iii), the entire initial binary parameter space favors the formation of a rotating remnant on energetic grounds alone, while only the highly relativistic regime of the binary parameter space of model (ii) has $\mathcal{M} > 0$. This narrows down the possible initial binary configurations that might lead to the formation of a rotating remnant. Furthermore, for the formation, we must require that the orbit of the inspiral contains sufficient angular momentum, i.e., condition 2. in (14) dictates that

$$|J_{\text{orb.}}| > |J_{\text{rot}}|. \quad (18)$$

This restricts the binary orbit to a subset of all possible inspirals. In fact, as we discuss below in Sec. III C, it is not necessary for (18) to be strictly satisfied, and furthermore there is also an upper bound on $J_{\text{orb.}}$ for the successful formation of a rotating remnant star, which we determine empirically below for an example inspiral.

According to the stability condition (15), the remnant rotating BS (or PS) must be a linearly (and non-linearly) stable solution. Despite the recent progress in understanding the stability properties of these rotating solutions, this is a subtle point, and we simply state that so far, no linear or nonlinear instability is known to exist in the parts of the rotating BS and PS parameter space we are interested in (see Figure 7 for an indication where known instabilities may be active). Finally, the last condition—the vortex condition—defined in (16), dictates that at the point of contact of the non-spinning binary, there must exist a $|q| = 1$ vortex in the phase in the vicinity of the center of mass of the system. This will be determined by the relative phases of the binary constituents. With these restrictions in hand, we are now

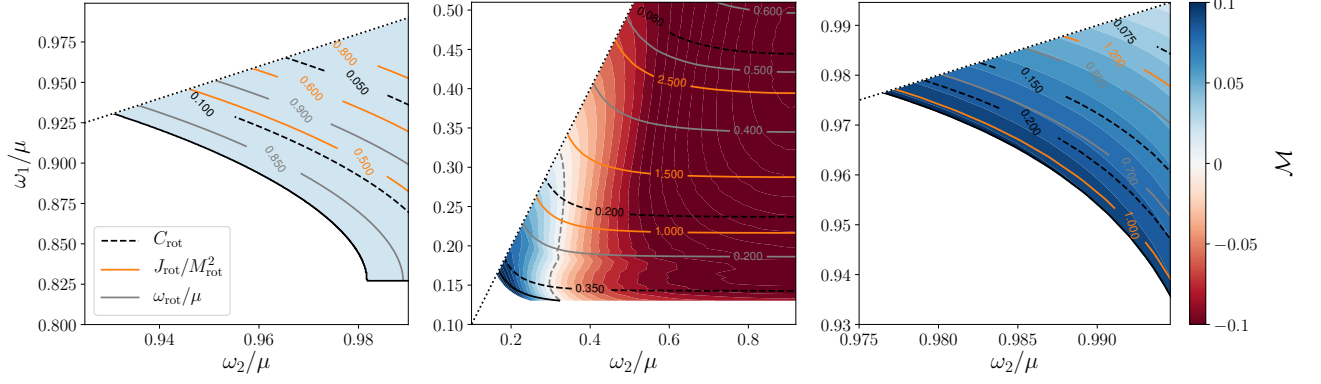


Figure 7. We plot the properties (dimensionless angular momentum $J_{\text{rot}}/M_{\text{rot}}^2$, frequency ω_{rot} , and compactness $C_{\text{rot}} = M_{\text{rot}}/R_{\text{rot}}$) of a $m = 1$ rotating remnant star, assuming the remnant map (13), as a function of the initial non-spinning BS frequencies ω_1 and ω_2 (contour lines). In addition, we show the normalized mass difference $\mathcal{M} = (M_1 + M_2 - M_{\text{rot}})/(M_1 + M_2)$ across the binary star parameter space (contour plot). Notice, the plot is symmetric under the interchange $\omega_1 \leftrightarrow \omega_2$, and we only consider the regime where $Q_1 + Q_2 < Q_{\text{rot}}^{\text{max}}$. (left) The binary parameter space in the repulsive scalar model with $\lambda/\mu^2 = 10^3$, (middle) the solitonic self-interactions with $\sigma = 0.05$, and (right) in the massive vector model without self-interactions. We explicitly restrict to only the radially stable Newtonian branches in the left and right panels, and the radially stable relativistic branch in the middle panel. In the middle, the dashed gray line indicates where $\mathcal{M} = 0$. Notice, for a $\sigma = 0.1$ solitonic scalar theory, no region with $\mathcal{M} > 0$ exists. The non-axisymmetric linear instability found in Ref. [55] is likely absent in the right panel; however, it is present in the middle for all $\omega_{\text{rot}}/\mu > 0.5$, and may be present in the left panel for some solutions with $\omega_{\text{rot}}/\mu < 0.9$, as shown in Ref. [57].

able to explicitly determine whether a rotating remnant star is formed dynamically, when all the above conditions are met, in the next section.

B. Formation dynamics

Consulting the remnant map shown in Figure 7, we begin by constructing non-spinning binary BS initial data that satisfies the conditions of the previous section. Here, we focus exclusively on the repulsive and solitonic scalar models, with $\lambda/\mu^2 = 10^3$ and $\sigma = 0.05$, respectively, and return to a discussion of the vector case below. In order to ensure that the vortex condition (16) is satisfied at the point of contact, we restrict to a binary made up

Model	ω_{sph}/μ	J_0/Q_0	x_0/M_0	y_0/M_0	v_x	v_y	α
repulsive	0.95	2.12	± 15	± 10	∓ 0.06	± 0.02	π
solitonic	0.25	1.16	± 20	± 3	∓ 0.3	0	π

Table II. The properties of non-spinning binary BS initial data leading to the formation of a rotating BS remnant. The two stars are identical, i.e., $\omega_1 = \omega_2 = \omega_{\text{sph}}$, with initial phase offset α , are positioned at coordinate locations x_0 and y_0 (upper signs refer to the first star), and have boost velocities v_x and v_y . The initial orbital angular momentum is J_0 , the ADM mass is M_0 , and Q_0 refers to the initial $U(1)$ -charge of the binary. The couplings are $\lambda/\mu^2 = 10^3$ and $\sigma = 0.05$ for the repulsive and solitonic scalar models, and the compactness of these stars is $C = 0.037$ and $C = 0.13$ in each of the models, respectively.

of identical stars, i.e., $\omega_1 = \omega_2 = \omega_{\text{sph}}$, but with opposite initial phase, $\alpha = \pi$. The remaining characteristics of the initial data are summarized in Table II. The frequency of the non-spinning stars are chosen to satisfy the kinematic and stability conditions. Specifically, comparing the properties presented in Table II with Figure 7, it is evident that these binaries satisfy $\mathcal{M} > 0$, and hence condition (17), and are in regions of the rotating BS parameter space without any known instabilities. The initial positions and velocities are set up in order to force the binary on a highly elliptical orbit and merge during the first encounter. The boost velocities are chosen to achieve sufficient angular momentum to form the rotating remnant star predicted by the remnant map: $J_{\text{rot}}/M_{\text{rot}}^2 = 0.56$ and $J_{\text{rot}}/M_{\text{rot}}^2 = 0.95$ for the stars in the repulsive and the solitonic scalar models, respectively. This ensures that condition (18) is satisfied at the point of contact. Finally, the center of mass of these binaries exhibits a $q = 1$ vortex throughout the evolution (measured with respect to the orbital angular momentum), by virtue of $\omega_1 = \omega_2$ and initial phase-offset $\alpha = \pi$, hence, satisfying the vortex condition (16). The details of the numerical construction of the constraint satisfying initial data are given in Appendix D.

In Figure 8, we show a few snapshots from the numerical evolution of the two sets of binary BSs constructed above, as well as the time evolution of the azimuthal mode decomposition of the real part, $\Phi_R = \text{Re}(\Phi)$, of the scalar field around the center of mass, and along the

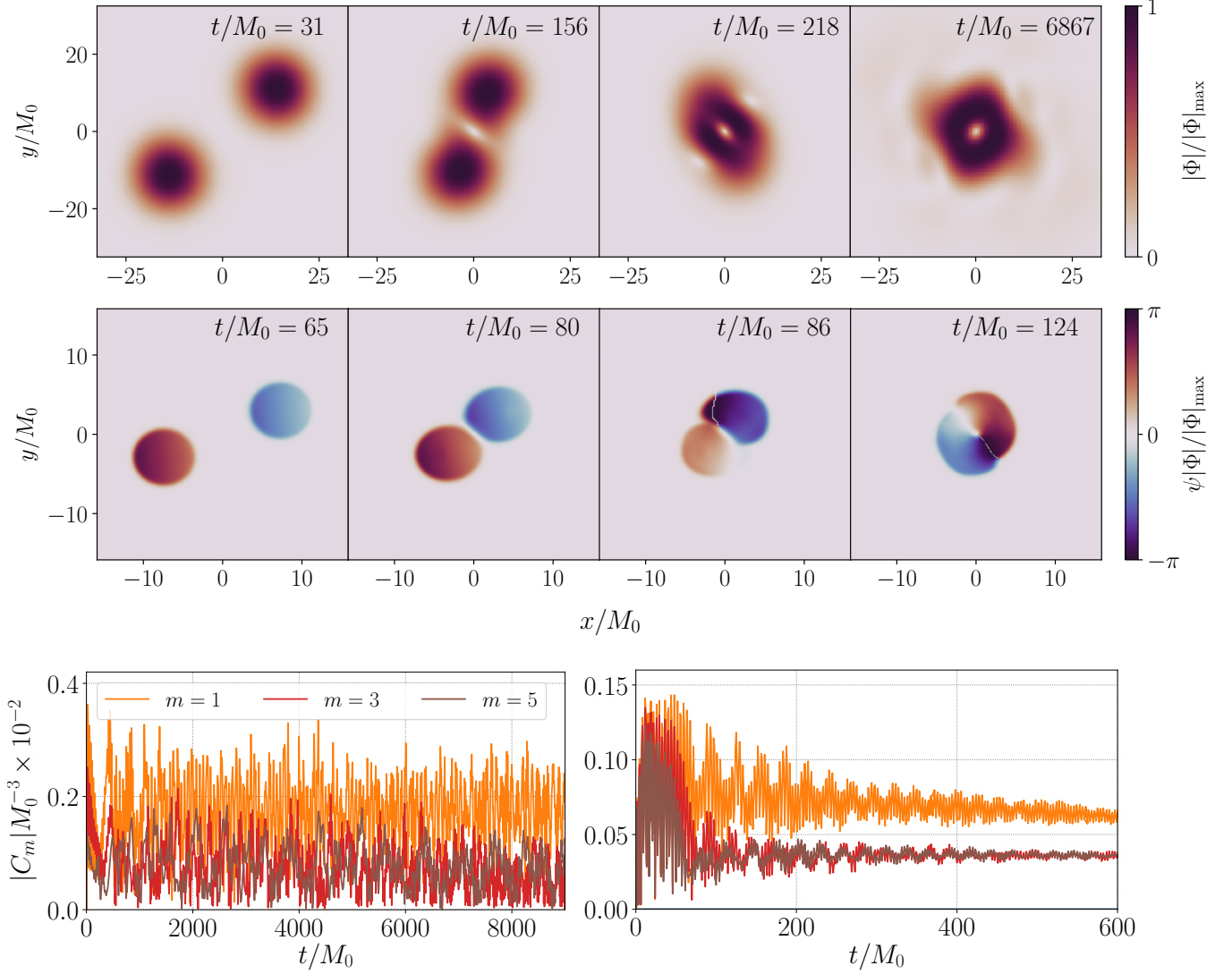


Figure 8. We illustrate the dynamics leading to the formation of $m = 1$ rotating BS remnants from the merger of two non-spinning BSs. (*top row*) Here, we focus on the binary star in the repulsive scalar model described in Table II. We show the magnitude of the scalar field normalized by the maximum magnitude $|\Phi|/|\Phi|_{\max}$ in the equatorial plane at four different times during merger. (*middle row*) We plot the product of the scalar phase ψ and the maximum normalized scalar field magnitude $\psi|\Phi|/|\Phi|_{\max}$ in the equatorial plane at four different times during the merger. Here, we show the binary in the solitonic scalar theory with properties given in Table II. (*bottom row*) The evolution of odd- m components of the azimuthal decomposition (19) of both binary mergers (the repulsive binary on the left, and the solitonic binary on the right). Notice, in the case of the solitonic binary, we show in Appendix D that the $m = 3$ and 5 modes are dominated by truncation error at late times and converge to zero. The even- m modes are negligible throughout the evolution.

angular momentum direction

$$C_m = \int d^3x \Phi_R e^{im\varphi}. \quad (19)$$

In the early stages of the evolution, $t/M_0 < 80$ and $t/M_0 < 150$, for the solitonic and repulsive cases, respectively, the phases of each stars evolve approximately linearly in time. At the point of contact, the scalar and gravitational interactions are highly nonlinear. During this merger phase, the scalar matter attaches to the vor-

tex line at the center of mass, and the system rings down to a state characterized by a single $m = 1$ mode in the scalar field—a rotating BS remnant. All other modes decay away over time. From the harmonic time-dependence of $\text{Re}(C_1)$, we obtain the late-time rotating remnant frequency of $\omega_{\text{rot}} M_0 = 0.78$ in the solitonic case. This is well approximated by the remnant map shown in Figure 7, which predicts $\omega_{\text{rot}} = 0.75/M_0 = 0.22\mu$, with the difference being attributable to the (Richardson-extrapolated) charge loss of $\Delta Q/Q_0 = 0.04$ occurring during merger,

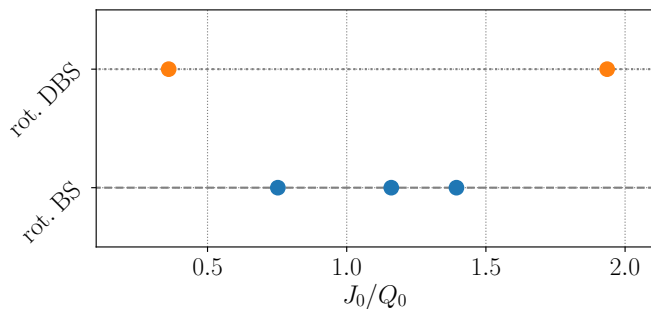


Figure 9. We classify the remnants of the mergers of a non-spinning binary BS into rotating DBS and rotating BS solutions as a function of the total (initial orbital) angular momentum J_0 . The angular momentum is normalized by the $U(1)$ -charge of the binary Q_0 .

as shown explicitly in Appendix D.

This explicitly demonstrates that, indeed, rotating BSs can be formed from the merger of two non-spinning BSs, given the conditions in Sec. III A are met. In particular, in the following section, we show explicitly that (at least approximately) satisfying the vortex condition is crucial for successfully forming the rotating remnant. In the case of the formation of rotating PSs (instead of BSs), the vector phase may play a similarly important role. However, these solutions also possess an intrinsic preferred direction (due to the vector field), and hence, the merger dynamics might not only be governed by the vector phase, but also the vector direction.

C. Robustness of formation mechanism

Having demonstrated the dynamics leading to the formation of rotating BSs from the merger of two non-rotating stars in several cases, we now analyze the robustness of this formation channel to variations in both the total angular momentum and the phase offset of the binary. To that end, we focus on the binary BS in the solitonic scalar model we found to form a rotating BS remnant in the previous section, and vary its initial angular momentum and phase offset, while keeping all other parameters, in particular, the $U(1)$ -charge, fixed. We show that there exists a set of binary BS initial data with non-zero measure that form a rotating BS remnant, demonstrating the robustness of the formation mechanism.

1. Variation of angular momentum

To quantify the robustness of the formation channel to variations in the binary angular momentum, we perform a series of simulations of the solitonic binary BS specified in Table II with varying initial boosts $|v_x| \in \{0.1, 0.25, 0.3, 0.35, 0.45\}$. This changes the initial an-

gular momentum J_0 away from the value of the binary specified in Table II. We evolve these sets of initial data through merger (see Appendix B for snapshots of the evolution). In Figure 9, the remnant of the merger is classified as either a rotating DBS solution (consisting of two orbiting, non-spinning stars, as described in Secs. II B and II E), or a $m = 1$ rotating BS solution. While both remnant classes possess a $|q| = 1$ vortex at the center of mass, the scalar field magnitude morphology is distinct; rotating BS solutions are stationary and exhibit toroidal surfaces of constant scalar field magnitude, in contrast to rotating DBS solutions, which exhibit two disconnected surfaces of constant scalar field magnitude⁶. Notice also, the rotating DBS remnant is *not* a stationary solution, as it continues to radiate energy and angular momentum. Consulting Figure 9, a variation of the initial angular momentum of up to $\Delta J_0/Q_0 \approx \pm 50\%$ still leads to the prompt formation of a rotating BS remnant⁷. However, if $|\Delta J_0|/Q_0$ is above some critical threshold (shown in Figure 9), then the system settles temporarily into a rotating DBS solution with long orbital period if $\Delta J_0 < 0$, and short orbital period if $\Delta J_0 > 0$. If both the initial angular momentum J_0 and total charge Q_0 of the binary system were conserved through merger, then only the initial data satisfying $J_0 = Q_0$ could form a $m = 1$ rotating remnant. However, due to scalar and gravitational radiation, both angular momentum and $U(1)$ -charge may be carried away from the system resulting in the formation of a rotating BS remnant for initial data with a range of initial angular momenta. For instance, based on the scalar field morphology, we find the binary configuration with $J_0/Q_0 \approx 0.75$ (shown in Figure 9) to settle into rotating BS after merger (see also Figure 16). This highly perturbed remnant plausibly continues to emit residual energy and $U(1)$ -charge, approaching $J/Q \approx 1$ at late times. Furthermore, the rotating DBS remnant with $J_0/Q_0 \lesssim 0.5$ may settle into a non-rotating DBS solution as suggested in Sec. II E, while the spinning DBS remnant with $J_0/Q_0 \gtrsim 1.5$ could plausibly settle into either a non-rotating DBS solution or a rotating BS as the system radiates angular momentum. Ultimately, the formation mechanism is robust against variations of binary orbital angular momentum to the degree shown in Figure 9.

2. Variations of scalar phase

Thus far, we have tested the robustness of the formation of a rotating BS from merger by varying the initial angular momentum of the binary BS's orbit, while

⁶ A more robust method to identify the remnants as rotating BSs (opposed to rotating DBSs) is to, for instance, explicitly check the consistency of $J_{\text{rem}} = mQ_{\text{rem}}$ of the remnant solution at late times (satisfied only by rotating BSs).

⁷ Note, the initial angular momentum J_0 is determined using the gauge-dependent “ADM” angular momentum of the initial data.

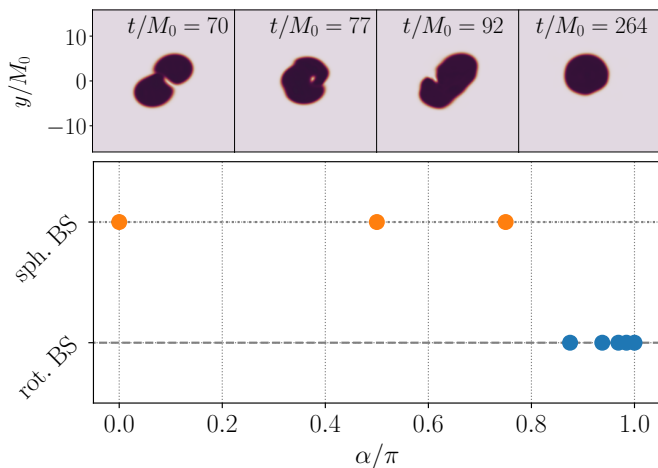


Figure 10. (*top*) We show the normalized magnitude of the scalar field $|\Phi|/|\Phi|_{\max}^{t=0}$ in the equatorial plane at four different times during the evolution of the binary BS merger with parameters given in Table II, but with initial phase-offset $\alpha/\pi = 3/4$. (*bottom*) We classify the remnant solution of binary BSs with different values of the initial phase α into spherical or rotating ($m = 1$) BSs. We consider $\alpha/\pi \in \{1, 63/64, 31/32, 15/16, 7/8, 3/4, 1/2, 0\}$.

keeping the initial scalar phase-offset between both stars fixed, i.e., $\alpha = \pi$. In this section, we fix $J_0/Q_0 = 1.16$ and instead vary the initial phase-offset between the two solitonic stars α . Hence, we consider binary mergers in the solitonic scalar model with parameters given in Table II, but with different initial phases $\alpha/\pi \in [0, 63/64]$. We demonstrated in Sec. III B that the $\alpha/\pi = 1$ case results in the formation of a $m = 1$ rotating BS remnant. The $\alpha = 0$ binary promptly leads to the formation of a *non-rotating* BS remnant, shedding all its orbital angular momentum. Hence, there exists a critical value, $0 < \alpha_{\text{crit}} < \pi$, for which the remnant is marginally either a non-spinning or a rotating BS remnant.

In the bottom panel of Figure 10, we classify the remnants of the merger of the sequence of these binary BSs with varying initial phase into spherical and rotating BSs. We find all binaries with $\alpha/\pi \geq 7/8$ form a $m = 1$ rotating remnant at late times, while all binaries with $\alpha/\pi \leq 3/4$ result in a non-rotating BS remnant⁸. We find all remnant rotating stars persist, without further sign of instability, for the remainder of the evolutions of length $t \gtrsim 1000M_0$.⁹ Therefore, the formation scenario

discussed in Sec. III A does not require the phase offset of the merging binary to be fine-tuned, and is robust up to a phase variation of $|\Delta\alpha|/\pi \approx 0.12$ around $\alpha/\pi = 1$. In the top panel of Figure 10, we show a few snapshots of the evolution of the binary with $\alpha/\pi = 3/4$. In the first panel, the vortex is located to the right of the center of mass during the initial contact of the stars. The vortex then traverses the merging object in the second panel and is ejected in the third panel. The final state (fourth panel) is a perturbed non-rotating BS. This behavior is representative of all cases with $1/2 \leq \alpha/\pi \leq 3/4$. In the $\alpha = 0$ limit, any vortex present due to the non-vanishing orbital angular momentum stays *outside* the remnant star altogether.

D. Formation channel

In the previous sections, we demonstrated that rotating BSs can be formed from the merger of two non-spinning stars without fine tuning of the binary parameters for several examples. In this section, we consider more generally for what systems the approximate conditions for the formation of a rotating BS remnant listed in Sec. III A are satisfied, and its implications for different formation channels for rotating BSs. We focus exclusively on binary mergers, and do not discuss, for example, formation of a rotating star from the collapse of coherent rotating cloud (as in, e.g., Ref. [55]).

First, from Figure 7, it is clear that the energy condition (17) is not restrictive for the repulsive scalar model and PSs (since $\mathcal{M} > 0$ across the parameter space). However, this condition does restrict the solitonic scalar theory to a small $M_1/M_2 \sim \mathcal{O}(1)$ region in the highly relativistic part of the stable branch of the families of stars. Therefore, while in the former two models, the formation of a rotating star is possible in the entire parameter space, including the Newtonian limit, the situation is more complex in the solitonic scalar model. There, a spherical star would first have to be formed in the relativistic part of the family of BSs (i.e., in the region of parameter space in Figure 7 where $\mathcal{M} > 0$). If a star is formed on the Newtonian branch of the non-spinning solutions within the solitonic scalar model, then it can move towards the relativistic branch by gaining mass (e.g., through a sequence of binary BS mergers), which generically leads to a more compact, i.e., more relativistic, remnant. Once these stars have migrated to the relativistic branch, the formation of a rotating BS remnant is possible from a relativistic binary with mass-ratio close to unity.

Secondly, the stability condition (15) is the most restrictive, as all known $|m| > 1$ rotating BSs are linearly unstable [55, 57, 58], allowing only the formation of $m = 1$ rotating BS remnants in scalar models *with* self-interactions (i.e., in the limit of vanishing scalar self-interactions, all $m = 1$ BSs are likely linearly unstable). Furthermore, in the case of attractive scalar self-interactions (i.e., the solitonic scalar model), even the

⁸ As another illustration of this type of behavior, we also considered the binary BS in the repulsive scalar model characterized in Table II, with initial phase-offset $\alpha/\pi = 7/8$; this binary tends towards a non-rotating BS remnant at late times after merger.

⁹ We note that at lower numerical resolutions, the rotating remnant formed when $\alpha/\pi \geq 7/8$ appears to have a growing perturbation that eventually ejects the central vortex from the star. However, this behavior disappears at sufficiently high resolutions. Details can be found in Appendix E.

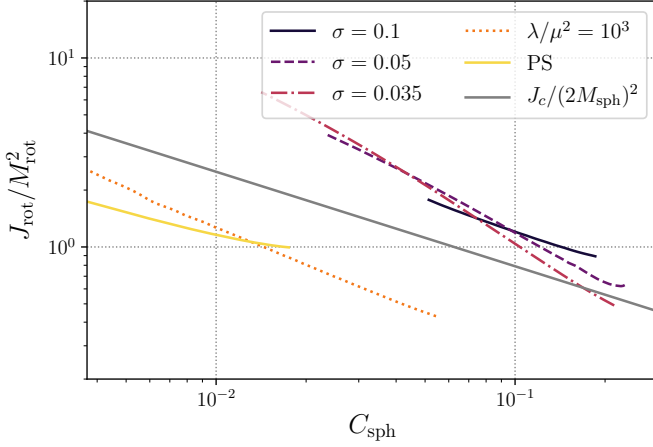


Figure 11. As a function of the compactness C_{sph} of two identical non-rotating stars in various models and couplings, we compare the dimensionless angular momentum of the corresponding $m = 1$ rotating BS and PS solution obtained using the remnant map (13). In particular, we compare three families of stars in the solitonic scalar model of coupling strength σ with the family of PSs, scalar BSs in the repulsive scalar model (labelled with its coupling λ), and the Newtonian quasi-circular angular momentum at the point of contact J_c , derived in the main text. We focus only on the solution branches below the maximum mass. Notice, however, that not all the solitonic cases that are plotted lie in the stable part of the $m = 1$ rotating BS parameter space.

$m = 1$ BSs are linearly unstable in the Newtonian limit [58] and unstable to the ergoregion instability in the relativistic limit [9, 88], implying that in the solitonic model *only* those non-spinning stars in the relativistic part of the parameter space may form rotating BS remnants *without* ergoregions during merger. In the case of the repulsive scalar model (with sufficiently strong self-interactions), all $m = 1$ rotating BSs below the maximum mass of the family of solutions are linearly stable [57, 58]. The $m = 1$ rotating PSs were shown to be linearly stable using numerical simulations in [55], suggesting that also rotating PSs may be formed across a large part of the parameter space. The $m = 1$ rotating solutions in the repulsive scalar models and the massive vector theory exhibit ergoregions only near the maximum mass and in the strong coupling limit, only marginally affecting the parameter space in which the formation of a rotating remnant is possible.

Lastly, the angular momentum condition (18), restricts the types of orbits that could lead to a rotating remnant BS. In the following, we focus entirely on the equal mass limit of the inspiral binary for simplicity. In the Newtonian limit, a compact binary, composed of two point masses M_{sph} on circular orbits with separation d and orbital frequency $\Omega = \sqrt{2M_{\text{sph}}/d^3}$, possesses orbital angular $J_{\text{orb}} = \nu\Omega d^2$ with reduced mass $\nu = M_{\text{sph}}/2$. Furthermore, if each compact object has a radius R_{sph} and compactness $C_{\text{sph}} = M_{\text{sph}}/R_{\text{sph}}$, then the angular mo-

mentum of the binary, at the point of contact of the two objects, is $J_c = M_{\text{sph}}^2/\sqrt{C_{\text{sph}}}$. For a typical non-spinning neutron star, $C_{\text{sph}} = 0.125$, the dimensionless orbital angular momentum at contact is $J_c/(2M_{\text{sph}})^2 = 0.7$, which is roughly consistent with non-linear simulations [86, 87]. In Figure 11, we compare this quasi-circular orbit estimate J_c to the spin angular momenta of four families of $m = 1$ BSs and the family of $m = 1$ PSs as a function of the compactness of the equal mass non-spinning binary they emerge from using the remnant map (13). From Figure 11, it is clear that the rotating non-relativistic stars (those in the repulsive scalar model and the PSs) require far less angular momentum than a quasi-circular orbit would provide, while on the other hand, the rotating relativistic stars (those in the scalar theory with solitonic potential) require far more angular momentum than a quasi-circular orbit could provide. While our estimate is purely Newtonian, and compares only the dimensionless spin at the point of contact (i.e., neglects radiation emitted during the merger process), it provides a rough estimate for the parameter space, where rotating BSs may form through quasi-circular inspirals. Therefore, from Figure 11 we conclude that in the solitonic and repulsive scalar models, as well as in the case of PSs, a quasi-circular orbit is unlikely to lead to the formation of a rotating remnant BS, with exceptions only in isolated and small parts of the parameter space.

Due to the non-relativistic nature of this estimate, there may be highly relativistic rotating solitonic BSs that could be formed through quasi-circular orbits, or the possibility that scalar interactions between diffuse repulsive stars radiate sufficient angular momentum during the late inspiral and merger leading to a rotating BS remnant. For instance, the binary inspiral in the repulsive scalar model shown to result in a rotating remnant BS in Sec. III B possessed an oversupply of angular momentum, i.e., $J_0/Q_0 = 2.12$, and yet formed a (highly perturbed) $m = 1$ rotating BS remnant. This may similarly hold for merging PSs. However, it appears that the types of orbits that may robustly lead to the formation of a rotating remnant are relativistic, highly eccentric encounters of non-spinning relativistic stars in the solitonic scalar model, while only those stars with non-relativistic velocities and mild impact parameters may merge into rotating remnant PSs and BSs in the repulsive scalar model.

E. Merger of mixed spinning-non-spinning BS binaries

To further understand the formation of a rotating BS remnant from the merger of two isolated BSs, we now turn to mergers of binaries consisting of a non-spinning and a $m = 1$ spinning star. In this scenario, one can use the mass-ratio $\tilde{q} = M_{\text{rot}}/M_{\text{sph}}$, or equivalently the charge-ratio $\tilde{\zeta} = Q_{\text{rot}}/Q_{\text{sph}}$, to classify the system as an equal mass-ratio, $\tilde{q} \sim 1$, or extreme mass-ratio, $\tilde{q} \ll 1$ and $\tilde{q} \gg 1$, system. The types of BSs we consider here are

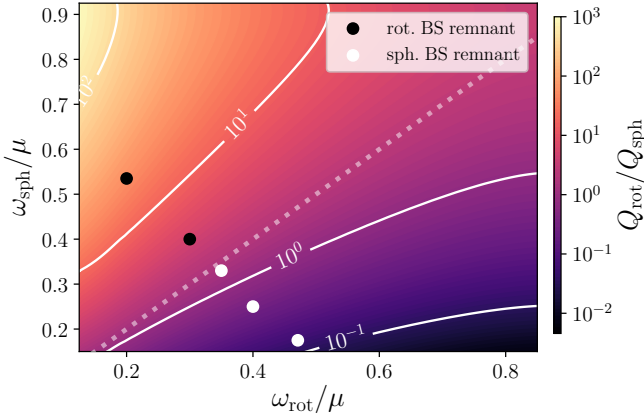


Figure 12. We plot the mass ratio $\tilde{q} = M_{\text{rot}}/M_{\text{sph}}$ (white contour lines) and charge ratio $\tilde{\zeta} = Q_{\text{rot}}/Q_{\text{sph}}$ (color) across the parameter space of a (superposed) binary BS consisting of a non-spinning star with frequency ω_{sph} and an $m = 1$ rotating star with frequency ω_{rot} in the $\sigma = 0.05$ solitonic scalar model. The dashed white line indicates where $\omega_{\text{sph}} = \omega_{\text{rot}}$. The mergers of binaries with parameters indicated by the black (white) points result in a single rotating (non-rotating) BS remnant.

perturbatively stable against known instabilities. Hence, in the $\tilde{q}, \tilde{\zeta} \rightarrow \infty$ limit, we expect the non-rotating star to be a small perturbation to the spinning star, and thus for the remnant to be spinning (i.e., the only relevant vortex line is that of the spinning star). Conversely, in the $\tilde{q}, \tilde{\zeta} \rightarrow 0$ limit, the remnant will be a non-spinning BS (hence, the vortex line of the spinning star is perturbative and neglected in the vortex condition (16)). This is entirely consistent with the expectation based on the remnant map introduced in Sec. II E. In the intermediate regime, where $\tilde{q}, \tilde{\zeta} \sim 1$, the importance of the vortex from the spinning BS is ambiguous, and therefore, and the application of the remnant map is less clear. Instead of assuming the accuracy of the remnant map, here we simply perform a series of non-linear simulations of binary BSs in the solitonic scalar model with coupling $\sigma = 0.05$, covering the range of mass-ratios from $\tilde{q} = 22$ to $\tilde{q} = 0.15$.

ω_{rot}/μ	ω_{sph}/μ	$\tilde{q} = M_{\text{rot}}/M_{\text{sph}}$	$\tilde{\zeta} = Q_{\text{rot}}/Q_{\text{sph}}$
0.20	0.535	22	63
0.30	0.40	3.9	4.6
0.35	0.33	1.5	0.95
0.40	0.25	0.51	0.30
0.471	0.175	0.15	0.06

Table III. The constituent BS frequencies, mass ratios, and charge ratios of the mixed spinning-non-spinning binary BS initial data discussed in the main text. The two stars have frequencies ω_{rot} and ω_{sph} , (purely tangential) boost velocities $v_{\text{rot}} = 0.85M_{\text{sph}}v_t/M_0$ and $v_{\text{sph}} = -0.85M_{\text{rot}}v_t/M_0$ with $v_t = \sqrt{M_0/D_0}$, and coordinate separation $D_0 = 10M_0$, in units of the ADM mass.

We summarize the properties of the constructed initial data in Table III.

In Figure 12, we show the parameter space of such binary BSs consisting of one rotating and one non-rotating constituent together with the merger product of the binaries characterized in Table III. By construction, the binaries merge after roughly one orbit in all cases considered. During the merger of the three cases with smallest mass-ratio, the vortex of the lighter spinning star is ejected from the system at the point of contact or shortly after. The merger dynamics become more violent with increasing initial mass-ratio, up to $\tilde{q} \sim 1$. The endstate in all three cases is a single, non-rotating star, while in the $\tilde{q} = 1.5$ case, a small scalar clump is ejected from the system similar to what was found in Ref. [44]. The two cases with largest mass- and charge-ratios merge into a single rotating BS remnant, identified by the $q = 1$ vortex at the center of the remnant star. The remnant star of the $\tilde{q} = 22$ binary persists for $t \gtrsim 600M_0$ without sign of instability, while the rotating remnant of the $\tilde{q} = 3.9$ remains non-perturbatively rotating for $t \approx 700M_0$. In the latter case, after this time in our simulation the central vortex is ejected in the same way as occurred at lower resolutions for the spinning remnant formed from the merger of non-spinning BSs described in Sec. III C (see Appendix E for details). Hence, we speculate that this is an artifact of the low resolution used to study this binary, and that at sufficiently high resolution simulations the star will remain stable after merger. However, we have not explicitly checked this for this case. In conclusion, we find that in the merger of a non-spinning and a rotating BS, the remnant is non-rotating roughly when the mass (or charge) ratio $\tilde{q} < 1$, and rotating when $\tilde{q} > 1$.

IV. DISCUSSION AND CONCLUSION

In this work, we have studied the inspiral and merger dynamics of a large class of scalar binary BS systems in representative repulsive and attractive scalar potentials. To that end, we constructed constraint satisfying binary BS initial data using the conformal thin-sandwich approach and numerically evolved these data using the coupled Einstein-Klein-Gordon equations. We reviewed important results on the non-gravitational interactions between two Q-balls, and identified the impact of such interactions on the GW phenomenology of an inspiraling binary BS. We pointed out the pivotal role the scalar phase and vortex structure plays during the inspiral and merger process of a binary BS. In particular, in the cases we study we find that (i) the scalar interactions secularly accumulate throughout the late inspiral and drive strong de-phasing and amplitude modulations of the gravitational radiation, (ii) during the merger of a binary BS the GW signal is strongly affected by vortex dynamics, and that (iii) the nonlinear scalar interactions induce a prolonged hypermassive BS phase, and can delay the col-

lapse to a black hole by several hundred light crossing times of the remnant, though do not strongly affect the final black hole’s mass and spin. These findings demonstrate that, to have a consistent description of the late inspiral for such models that accurately predicts the emitted GWs be taken into account. Analogous to axion mediated forces in the inspiral of a binary neutron star considered in Refs. [89–91], the de-phasing and amplitude modulations from scalar interactions may enter at lower orders in a perturbative post-Newtonian expansion of the binary dynamics compared to tidal Love number effects, and hence, be a strong handle to efficiently distinguish binary BS mergers from binary neutron star ones. Additionally, our results suggest that predicting the GWs emitted during the nonlinear merger process (and of a potential hypermassive BS remnant) for a large class of binary constituents requires a substantial suite of nonlinear numerical evolutions, since the GW phenomenology is likely richer than even in the case of binary neutron stars, due to the star’s internal scalar phase degree of freedom characterizing the merger. Lastly, if the final remnant of the merger is a black hole, then the ringdown GW signal may be indistinguishable from that of a binary black hole merger remnant (or a binary neutron star merger resulting in black hole formation) in all but the least compact cases. If the constituent stars of the binary are less compact than typical neutron stars, then we show that accreting residual matter surrounding the remnant black hole may alter the ringdown signal sufficiently to distinguish it from the typical exponential black hole ringdown GW signals. On the other hand, if the remnant is a BS (spinning or non-rotating), then the ringdown signal is likely an efficient means of distinguishing the types of binaries, particularly if the total mass of the system is $M_0 \gtrsim \mathcal{O}(10)M_\odot$ (positioning the ringdown GW signal in the most sensitive band of ground-based GW detectors).

Furthermore, in this work, we have constructed a remnant map, augmented by several conditions, which approximately predicts the remnant star that results from a binary BS merger. We illustrated the utility of this mapping to qualitatively predict the outcome of the nonlinear dynamics of merging BSs using a particularly peculiar spinning binary BS inspiral. This inspiral results in the formation of a rotating dipolar BS solution (see, e.g., Refs. [38, 77]), as predicted by the remnant map. We also briefly commented on the implications of the remnant map on PS dynamics. We emphasize the central role of the scalar phase and vortex structure during the merger of binary BSs. In other areas of physics, vortices also play an important role, leading to phenomenology such as vortex reconnection and vortex lattices [62–65]. These, and similar processes, may also arise in the context of BSs and are an interesting direction for the future. While the predictions of the remnant map are most accurate for equal frequency stars, we find it to be a decent approximation even in more complex scenarios. However, in a few merger examples, we explicitly show the

limitations of the remnant map. In particular, the classification of a vortex line as “significant” within the vortex condition is ambiguous. For instance, in the inspiral of a light spinning star and a heavy non-rotating star, the vortex line of the former must be classified as insignificant compared with the heavy companion in order for the vortex condition to be consistent with the formation of non-rotating remnant. However, as the relevant mass of the spinning star is increased, it is unclear, a priori, at exactly what mass ratio the vortex becomes significant to the remnant, and therefore there is no firm prediction for the exact threshold in the comparable mass regime where a rotating remnant will be formed. In this work, we primarily focused on the special case of a binary inspiral resulting in a single remnant star. However, this map could be extended to include more than two stars taking part in the merger and more than one remnant star.

Moreover, in this work we find, for the first time, examples where the merger of non-rotating stars results in the formation of a rotating BS. We achieve this by utilizing the remnant map paired with, in particular, the vortex condition, which is a crucial ingredient in understanding the formation of rotating BSs in mergers. We investigated the robustness of this new formation mechanism to changes in the binary’s orbital angular momentum and initial scalar phase-offset, finding that variations of up to a factor of two of the orbital angular momentum and up to 12% of the initial phase-offset still result in the formation of a rotating remnant star. Hence, a large set of binary configurations may form rotating remnant stars, rather than non-spinning BSs or black holes. Furthermore, we find that quasi-circular orbits may inhibit the formation of rotating remnant BSs, since these orbits have either too little angular momentum (in the case of the solitonic scalar potential), or too much angular momentum (in the case of PSs and for stars in the repulsive scalar model considered). However, our results suggest that there may be limited regions of parameter space where a quasi-circular orbit leads to the formation of a rotating remnant star. Finally, regarding the merger remnant of a binary made up of a spinning and a non-spinning star, the mass-ratio (or charge-ratio) is a decent classifier of the remnant product: if the non-spinning star is heavier, then the remnant is a non-rotating star, while if the spinning star dominates the mass-ratio, then the remnant will be a rotating BS. We also briefly comment on the implications of the formation mechanism on PS dynamics and the formation of rotating PSs after a binary inspiral. Previous attempts at forming a rotating BS or PS remnant from the merger of two non-spinning stars have been unsuccessful, as they violated one or several of the conditions found here. The mergers of binary BSs considered in Refs. [40, 42–44] violated the vortex condition or stability condition, while the orbital PS mergers considered in Ref. [48] violated, at the least, the kinematic and vortex conditions. Lastly, if an astrophysical population of these stars existed, then a subset

of the binary inspirals may form rotating BS remnants, provided the scalar self-interactions allow it. In fact, using our results, one could quantify how many rotating boson star may be formed given the characteristics of a population of non-spinning binary stars. This formation mechanism could be used to study the inspiral, merger, and ringdown dynamics of black hole mimicking ultra compact objects self-consistently in a nonlinear setting. In some cases, these rotating BS remnants are highly relativistic, exhibiting stable light rings and ergoregions. The impact of these features on the emitted gravitational waveform may be studied within these scenarios and extrapolated to a larger set of ultra compact objects.

ACKNOWLEDGMENTS

We would like to thank Luis Lehner for valuable discussions. We acknowledge support from an NSERC Discovery grant. Research at Perimeter Institute is supported in part by the Government of Canada through the Department of Innovation, Science and Economic Development Canada and by the Province of Ontario through the Ministry of Colleges and Universities. This research was undertaken thanks in part to funding from the Canada First Research Excellence Fund through the Arthur B. McDonald Canadian Astroparticle Physics Research Institute. This research was enabled in part by support provided by SciNet (www.scinethpc.ca), Compute Canada (www.computeCanada.ca), and the Digital Research Alliance of Canada (www.alliancecan.ca). Simulations were performed on the Symmetry cluster at Perimeter Institute, the Niagara cluster at the University of Toronto, and the Narval cluster at the École de technologie supérieure in Montreal.

Appendix A: Revisiting the non-axisymmetric instability of rotating boson stars

In this appendix, we briefly revisit the non-axisymmetric instability (referred to as NAI in the following) discovered in [55], focusing on the importance of the scalar phase and vortex structure in these solutions. To gain intuition, we re-analyze two unstable BSs with $m = 1$ and 2 , in the solitonic and repulsive scalar theories introduced in (4) and (5), respectively, originally considered in Ref. [57], and discuss the instability in light of the remnant map constructed in Sec. II E.

1. Instability of a $m = 2$ boson star

We begin with the phase evolution during the development and saturation of the NAI of a $m = 2$ rotating BS solution. Specifically, we evolve the $m = 2$ rotating BS of frequency $\omega/\mu = 0.4$ in the $\sigma = 0.05$ solitonic scalar

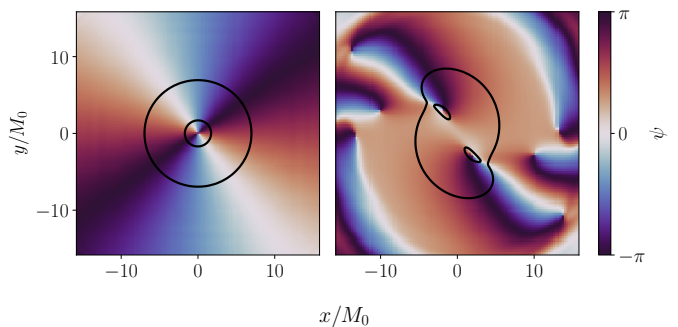


Figure 13. We show the scalar phase in two equatorial slices of the $m = 2$ rotating BS of frequency $\omega/\mu = 0.4$ in the $\sigma = 0.05$ solitonic scalar model undergoing the NAI (first discussed in Ref. [57]). The left panel shows the scalar phase at $t/M_0 = 0$, while the right panel shows the scalar phase during the nonlinear saturation of the NAI. The black lines indicate arbitrarily chosen level surfaces of the scalar field magnitude within the equatorial plane.

model in (4). The NAI of this stationary solution exhibits characteristic growth timescales of $\tau_{\text{NAI}}/M_0 \approx 19$, leading to the ejection of two blobs of scalar matter in opposite directions, leaving behind a single non-spinning remnant star at the center of mass (see panel b of Fig. 8 in Ref. [57] for snapshots of the saturation of the NAI in this star). In Figure 13, we show the scalar phase in the equatorial slice at the start of the evolution, and during the non-linear saturation of the NAI. Initially, the vortex at the center of the star is a $q = 2$ vortex (as expected for a $m = 2$ star). However, during the non-linear saturation of the NAI shown on the right in Figure 13, this $q = m = 2$ vortex at the center of mass breaks up into *two* $q = 1$ vortices, which are quickly ejected from the star, leaving only a non-spinning star at late times (not shown in Figure 13). This is reminiscent of, for instance, the break-up of a $m = 2$ string in the Abelian-Higgs model (see, e.g., Ref. [92]).

2. Instability of a $m = 1$ boson star

We turn now to the NAI active in a $m = 1$ rotating BS of frequency $\omega/\mu = 0.9$ in the repulsive scalar model with coupling $\lambda/\mu^2 = 10^2$. In the top panel of Figure 14, we show four snapshots of the evolution throughout the development and saturation of the NAI. At early times, the scalar field magnitude morphology is toroidal (first panel), while at intermediate times (second and third panel), the scalar field magnitude exhibits a quadrupolar pattern, which is broken up at late times (fourth panel) and eventually becomes a monopolar (i.e., perturbed spherically symmetric) remnant BS. It is clear from the top panel of Figure 14 that the $q = 1$ vortex of the stationary BS solution remains at the center of mass even during the *first* fragmentation (first and second panel) until the *second* fragmentation phase, when

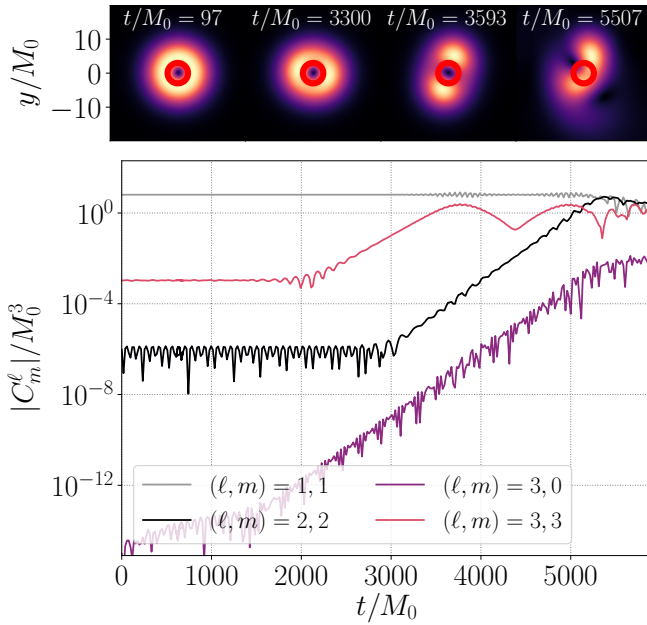


Figure 14. *(top)* We show the normalized scalar field magnitude $|\Phi|/|\Phi|_{\max}^{t=0}$ in four equatorial slices at different times during the evolution of an isolated $m = 1$ rotating BS of mass M_0 in the repulsive model with $\lambda/\mu^2 = 10^2$ and frequency $\omega/\mu = 0.9$. The star was shown to be unstable to the NAI in Ref. [57]. Red circles indicate the coordinate location of the vortex at early times in all snapshots. *(bottom)* The evolution of some of the spherical harmonic modes C_m^ℓ , defined in (A1), corresponding to the same star as in the top panel.

this vortex is ejected from the system (last panel).

In order to understand this two-staged fragmentation process, we decompose the scalar field $\Phi_R = \text{Re}(\Phi)$ into coordinate spherical-harmonic components C_m^ℓ as

$$C_m^\ell = \int_D d^3x \Phi_R Y_m^\ell(\theta, \varphi), \quad (\text{A1})$$

centered on the center of mass and aligned with the spin-axis of an isolated star. (Here, the domain of integration D is the ball of coordinate radius $r/M_0 = 25$). In the bottom panel of Figure 14, we show the evolution of some of the spherical harmonic components during the development and saturation of the NAI. First, the $(\ell, m) = (1, 1)$ component dominates throughout the evolution, since this is a $m = 1$ (toroidal) BS. Secondly, the even- m components are seeded roughly at the level of floating point roundoff at $t = 0$, while the odd- m components (except for $m = 1$) have amplitudes set by the truncation error (orders of magnitude larger than the floating point roundoff). While the even- and odd- m components shown in the bottom panel of Figure 14 all exhibit the same e-folding growth rate, suggesting that they are all associated with the same unstable mode, the NAI has a much larger overlap with the $(\ell, m) = (3, 3)$ component than the other components. During the first fragmentation phase around $t/M_0 \approx 3500$, the quadrupolar pat-

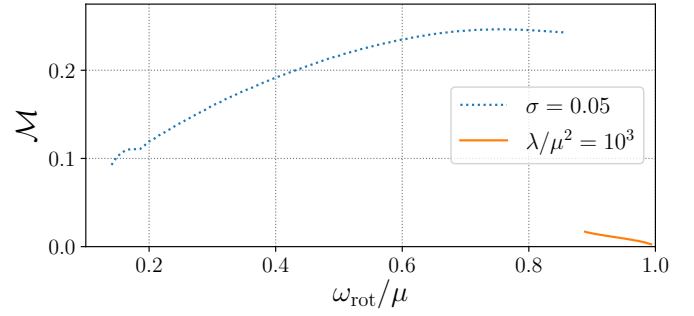


Figure 15. We show the normalized mass difference $\mathcal{M} = (M_* - M_{\text{rot}})/M_*$ between the mass M_{rot} of an isolated $m = 1$ spinning star of frequency ω_{rot} and a non-rotating star of mass M_* in the same models, when assuming the remnant map described in Sec. II E. We do this for the solitonic and repulsive scalar models, with couplings σ and λ , respectively. Therefore, for each ω_{rot} shown, \mathcal{M} indicates the energy gained by transitioning the $m = 1$ rotating star to a non-rotating star of the same charge. We show only the branches below the maximum mass of the families of solutions.

ter of $|\Phi|$ can be understood by considering the bottom panel of Figure 14. In this phase, the odd- m components dominant in the initial non-linear phase. In particular, the $(\ell, m) = (3, 3)$ perturbation mixes with the $(\ell, m) = (1, 1)$ background solution into a $\tilde{m} = 3 \pm 1$ mode of $|\Phi|$, corresponding precisely to the quadrupolar pattern observed in the top panel of Figure 14. During the second fragmentation around $t/M_0 \approx 5000$, the even- m components also become significant and their presence results in the ejection of the central vortex and the formation of the non-spinning, i.e., $m = 0$, BS remnant. The numerical convergence of this instability was checked in Ref. [57].

From this, we conclude that the NAI is dominated by odd- m perturbations of Φ_R and does not significantly affect the scalar vortex, even as the unstable mode starts to become large (and nonlinear). However, in the subsequent evolution in the nonlinear phase, even- m perturbations continue to grow and eventually lead to the ejection of the central vortex.

3. The instability and the remnant map

For completeness, we briefly discuss the transition from a $m = 1$ rotating BS to a non-spinning star of the same scalar model with the remnant map described in Sec. II E. This transition (similar to the NAI and its non-linear saturation) corresponds to the decay of a rotating solution to a non-rotating solution, which may be dynamically achieved by means of an instability in the $m = 1$ star. In Figure 15, show the energy gained by such a transition assuming the remnant map, i.e., assuming no scalar radiation. Clearly, it is energetically favorable to decay from a $m = 1$ rotating star to a non-rotating star. However, whether this is a hint of a linear instability everywhere

in the parameter space shown in Figure 15 is non-trivial. Furthermore, a dynamical transition requires the ejection of all angular momentum from the system, which may break the assumption of local charge conservation around the star. On the other hand, this demonstrates that the transition of two identical $m = 1$ BSs into two identical non-spinning stars is also energetically favorable, a scenario we explicitly found performing a nonlinear evolution in Sec. II E.

Appendix B: Angular momentum variation

In Figure 16, we present snapshots of the evolution of the sequence of non-spinning binary BSs of varying initial orbital angular momentum discussed in Sec. III C.

Appendix C: Isolated Proca star solutions

The details of the construction of isolated scalar BSs are presented in Ref. [57]. Hence, here we focus on our approach to constructing the PS solutions considered in this work. PSs are, analogous to scalar BSs, solutions to a massive complex field—in this case a vector field A_α of mass μ —minimally coupled to general relativity as [46]

$$S = \int d^4x \sqrt{-g} \left[\frac{R}{16\pi} - \frac{1}{4} F_{\alpha\beta} \bar{F}^{\alpha\beta} - \frac{1}{2} \mu^2 A_\alpha \bar{A}^\alpha \right]. \quad (\text{C1})$$

Here $F_{\alpha\beta} = \nabla_\alpha A_\beta - \nabla_\beta A_\alpha$ is the field strength, while the overbar denotes complex conjugation. This theory is also invariant under a global $U(1)$ transformation $A_\beta \rightarrow A_\beta e^{i\theta}$. The associated Noether current and Noether charge are

$$j^\mu = \frac{i}{2} (\bar{F}^\mu{}_\alpha A^\alpha - F^\mu{}_\alpha \bar{A}^\alpha), \quad Q = - \int d^3x \sqrt{-g} j^0, \quad (\text{C2})$$

respectively. The Lorenz relation, $\nabla_\alpha A^\alpha = 0$, is identically satisfied due to the antisymmetry in the field-strength, assuming $\mu \neq 0$ (and no vector self-interactions). The stress-energy associated with the action (C1) is given by

$$T_{\mu\nu} = -F_{\alpha(\mu} \bar{F}_{\nu)}^\alpha - \frac{1}{4} g_{\mu\nu} F^{\alpha\beta} \bar{F}_{\alpha\beta} + \mu^2 \bar{A}_{(\mu} A_{\nu)} - \frac{1}{2} \mu^2 g_{\mu\nu} A_\alpha \bar{A}^\alpha. \quad (\text{C3})$$

With this, the Einstein equations, sourced by the vector matter, and the vector field equations are given by

$$G_{\alpha\beta} = 8\pi T_{\alpha\beta}, \quad \nabla_\alpha F^{\alpha\beta} = \mu^2 A^\beta, \quad (\text{C4})$$

where $G_{\alpha\beta}$ is the Einstein tensor. Rotating PSs are asymptotically flat, axisymmetric solutions to the above system of equations. Hence, we make the ansatz

$$ds^2 = -f dt^2 + lf^{-1} \{ j(dr^2 + r^2 d\theta^2) + r^2 \sin^2 \theta (d\varphi - \Omega r^{-1} dt)^2 \}, \quad (\text{C5})$$

where f, l, j , and Ω are functions of r and θ . The corresponding ansatz for the vector 1-form is given by

$$\mathbf{A} = e^{i\omega t} (V dt + iB dr) \quad (\text{C6})$$

for spherically symmetric solutions, and

$$\mathbf{A} = e^{i\omega t} e^{im\varphi} \left(iV dt + \frac{H_1}{r} dr + H_2 d\theta + i \sin \theta H_3 d\varphi \right) \quad (\text{C7})$$

for rotating solutions. Here, in direct analogy to scalar BSs, this approach yields an infinite set of families of solutions indexed by their azimuthal mode m , and parameterized by their frequency ω . The boundary conditions for the vector field are $A_\mu \rightarrow 0$ for $r \rightarrow \infty$. However, in order to obtain non-trivial solutions to the field equations and these boundary conditions, we promote the frequency to a field $\omega \rightarrow \omega_s(r, \theta)$ and introduce the second auxiliary field $\rho(r, \theta)$, following Ref. [53], where this was applied in the scalar case (see also Ref. [57]). Both fields follow $\square_g = g^{\mu\nu} \nabla_\mu \nabla_\nu$ of the spacetime $g_{\mu\nu}$:

$$\square_g \omega_s = 0, \quad \square_g \rho = \frac{j^t}{\omega_s}. \quad (\text{C8})$$

Through the boundary conditions $\omega_s(r \rightarrow \infty) \rightarrow \omega$, where ω is the solution's frequency, we ensure that the solution is non-trivial. Integrating over the entire three-volume of a time-slice, we see that ρ encodes the total $U(1)$ -charge in its boundary data:

$$\lim_{r \rightarrow \infty} r^2 \partial_r \rho(r, \theta) = -\frac{Q}{4\pi\omega}. \quad (\text{C9})$$

Conversely, using (C9), we can impose Q as a boundary condition, and solve for ω_s . Hence, within this formalism, either the solution's frequency ω , or the solution's charge Q can be imposed as a boundary condition. The list of boundary conditions for the metric variables and auxiliary functions are given in Ref. [57], while the boundary conditions of the vector components are listed in Ref. [46]. One subtlety arises for $B(r)$ (in the spherically symmetric case), which follows a first order differential equation. We promote this equation trivially to a second order equation by $B(r) \rightarrow \partial_r \tilde{B}(r)$, and then impose the boundary condition $\lim_{r \rightarrow \infty} \tilde{B}(r) = \tilde{B}_\infty$ (the solution is independent of \tilde{B}_∞), while requiring $\partial_r \tilde{B}(r)|_{r=0} = 0$.

To numerically solve the system of equations introduced above subject to the boundary conditions, we follow the implementation for scalar BSs in Ref. [57]. We compactify the radial coordinate $r \rightarrow \bar{r} = r/(1+r)$, such that $\bar{r} \in (0, 1)$, and restrict to the upper-half plane, i.e., $\theta \in (0, \pi/2)$. We utilize fifth-order accurate finite differences both in the radial and polar directions, and consider a uniformly spaced grid in the compactified coordinates (\bar{r}, θ) . We utilize a Newton-Raphson-type relaxation procedure that iteratively approaches the true solution given a sufficiently close initial guess. The initial guess is constructed from plots given in Ref. [93].

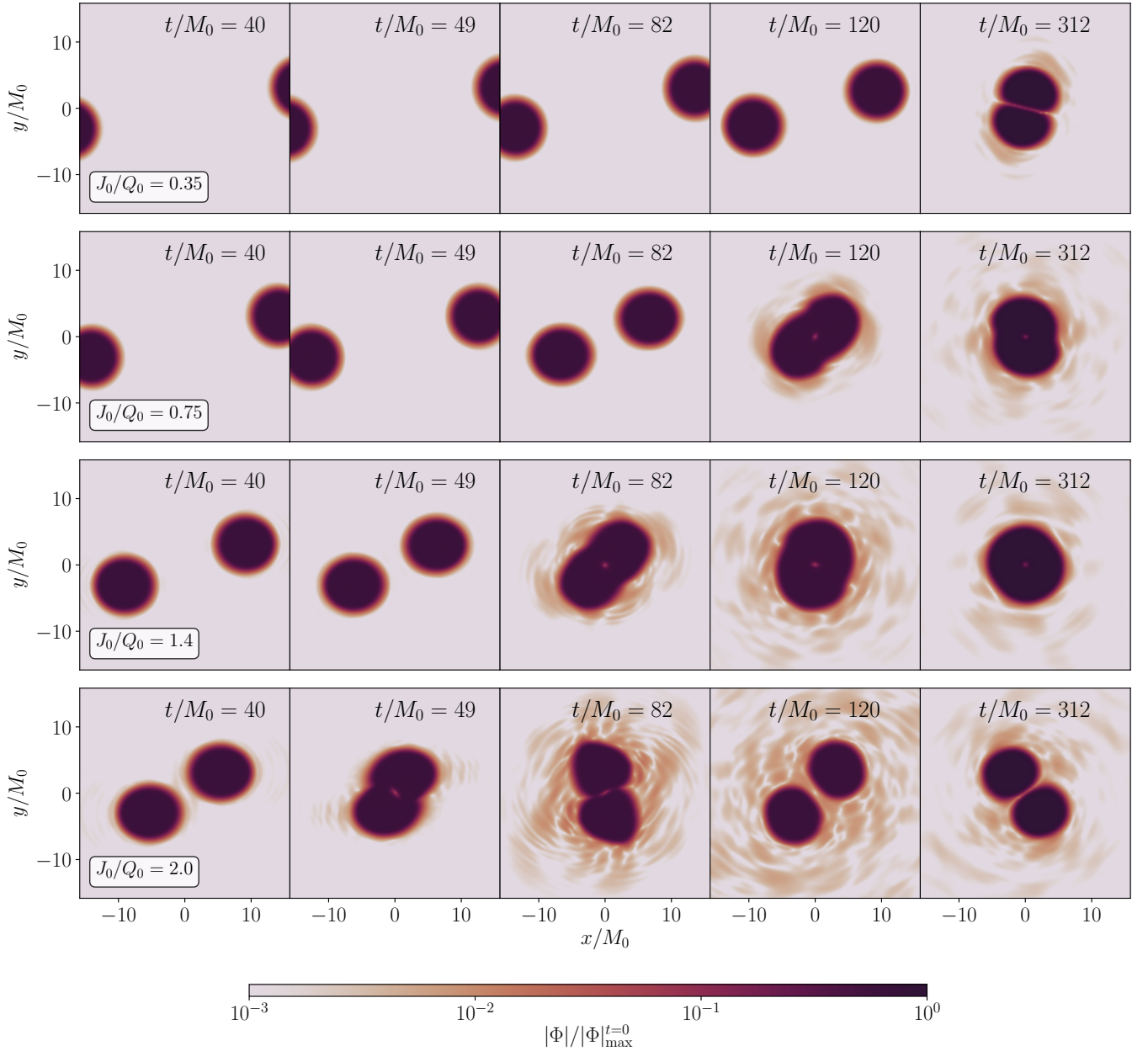


Figure 16. We show the scalar field magnitude $|\Phi|$ (normalized by the maximum in the initial time-slice) in a few snapshots of the equatorial slice of the binary BS simulations discussed in Figure 9. We label each sequence of time-slices by the initial angular momentum J_0 in units of initial charge Q_0 . In the top and bottom rows, the binary merges into a rotating DBS solution (i.e. two non-rotating BSs separated by scalar interactions, as discussed in Sec. II B). Compared with the top row, the binary in the bottom row rotates at high angular velocities around the center of mass at late times, i.e., $t/M_0 > 300$. The case shown in the middle two rows merge to form a remnant with $q = 1$ vortex at the center of mass at late times. Notice, we find that the $J_0/Q_0 = 0.75$ case relaxes to a rotating BS at late times $t/M_0 > 300$.

Once a solution is found at ω_1 , we explore the parameter space of each family m , by imposing the boundary conditions $\omega_2 = \omega_1 + \delta\omega$ (or analogously the vector charge), where $\delta\omega$ is chosen sufficiently small such that the solution at ω_1 is a good enough initial guess to obtain the solution at ω_2 . For spherically symmetric stars, we found that a resolution of $N_r = 1000$ was sufficient for all considered cases, while in the rotating case we typically use

$$N_r \times N_\theta = 500 \times 100.$$

Appendix D: Numerical setup

1. Initial data

In this work, we numerically evolve only scalar BSs. Hence, in what follows, we restrict ourselves entirely to the scalar case. In order to evolve a binary BS solution in general relativity consistently, we solve the Hamiltonian and momentum constraints of a superposed binary BS. Here, we only provide a brief summary of our procedure, and defer further details to Ref. [80]. We follow Ref. [94] and consider the constraint equations in the conformal thin-sandwich (CTS) formulation [95], where the spatial metric γ_{ij} on the initial time-slice is related to the conformal metric $\tilde{\gamma}_{ij}$ by the conformal factor Ψ :

$$\gamma_{ij} = \Psi^4 \tilde{\gamma}_{ij}. \quad (\text{D1})$$

Within the CTS framework, the extrinsic curvature $K_{ij} = -\mathcal{L}_n \gamma_{ij}/2$, defined by the Lie-derivative along the hypersurface normal \mathcal{L}_n , is decomposed into the trace-free part $A^{ij} = \Psi^{-10} \hat{A}^{ij}$ and the trace $K = \gamma_{ij} K^{ij}$. With the conformal lapse $\tilde{\alpha} = \Psi^{-6} \alpha$, Ricci scalar \tilde{R} associated with the conformal metric, the conformal covariant derivative \tilde{D}_i , and the matter energy and momentum densities E and p^i , the Hamiltonian and momentum constraint equations in the CTS formulation are

$$\tilde{D}^i \tilde{D}_i \Psi - \frac{\tilde{R}}{8} \Psi + \frac{\hat{A}_{ij} \hat{A}^{ij}}{8} \Psi^{-7} - \frac{K^2}{12} \Psi^5 = -2\pi \Psi^5 E, \quad (\text{D2})$$

$$\tilde{D}_j \hat{A}^{ij} - \frac{2}{3} \Psi^6 \tilde{D}^i K = 8\pi \Psi^{10} p^i. \quad (\text{D3})$$

We parameterize the energy and momentum densities as

$$E = \Psi^{-12} \tilde{\eta} \tilde{\eta} + \Psi^{-4} \tilde{D}^i \Phi \tilde{D}_i \Phi + V(|\Phi|), \quad (\text{D4})$$

$$p^i = -\Psi^{-10} (\tilde{\eta} \tilde{D}^i \Phi + \tilde{\eta} \tilde{D}^i \Phi), \quad (\text{D5})$$

where $\eta = \mathcal{L}_n \Phi$ and $\tilde{\eta} = \Psi^6 \eta$, following what was done in Ref. [96]. In addition to the usual conformal metric quantities that are free data in the CTS formalism, we specify Φ and $\tilde{\eta}$ (as opposed to a conformally rescaled energy and momentum density) as free data when solving the constraints.

Following Ref. [94], the free data for the CTS constraint equations is constructed from the plain superposition of the metric variables and scalar field degrees of freedom of two isolated star solutions:

$$\Phi = \Phi_{(1)} + \Phi_{(2)}, \quad \tilde{\eta} = \tilde{\eta}_{(1)} + \tilde{\eta}_{(2)}. \quad (\text{D6})$$

We displace and boost the isolated solutions along vectors $\beta_i^{(1)}$ and $\beta_i^{(2)}$ with coordinate velocity $v_{(1)}$ and $v_{(2)}$, respectively, prior to superposing the stars' solutions. The numerical construction of the isolated BS solutions used in this work is outlined in Ref. [57]. The elliptic constraint equations, subject to asymptotically flat boundary conditions, are then solved using Newton-Raphson relaxation combined with the multigrid method [94].

2. Numerical evolution

Given initial data for a scalar binary BS, we evolve the Einstein-Klein-Gordon equations (following from the scalar action (3)) forward in time employing the generalized harmonic formulation of the Einstein evolution equations [97]. To that end, we utilize fourth-order accurate finite difference stencils over a compactified Cartesian grid containing spatial infinity. There we impose asymptotically flat boundary conditions on the metric variables and set the scalar field to zero. This is paired with a fourth-order accurate Runge-Kutta time-integration. Of particular importance is the use of adaptive mesh refinement, with refinement ratio 2:1, to track the stars as they move across the Cartesian grid (see Ref. [98] for details). The compactness of the stars sets the number of levels required to resolve the stars sufficiently; for low-compactness solutions [typically stars in the repulsive scalar model, (5)], we require five to six refinement levels, while for the high-compactness solutions [usually those in the solitonic scalar model, (4)], we require six to seven levels. In the cases with black hole formation, we add refinement levels dynamically to resolve the gravitational collapse and apparent horizon (this requires seven to nine levels). The resolution on the finest mesh refinement level for the binary evolutions presented in Sec. IID is $\Delta x/M_0 = 0.15$. The resolution for the solitonic cases shown in Sec. IIIB is $\Delta x/M_0 = 0.075$ on the finest refinement level, while for the binaries in the repulsive model it is $\Delta x/M_0 = 0.2$. Throughout, we use the standard damped harmonic gauge condition to set the generalized harmonic source functions H_μ [34, 99].

3. Convergence tests

We present resolution studies of two exemplary binary mergers. First, we focus on the $\sigma = 0.05$ solitonic scalar model and the binary with parameters given in Table II. We consider three resolutions, corresponding to Δx , $3\Delta x/4$, and $\Delta x/2$, where the lowest resolution corresponds to a grid spacing of $\Delta x/M_0 \approx 0.1$ on the finest level, and the medium resolution is the default resolution for all simulations discussed in Sec. III. In order to explicitly demonstrate that we are solving the Hamiltonian and momentum constraints, we track the violations of the constraints, given by $C_\mu = H_\mu - \square x_\mu$, in time. In Figure 17, we plot the evolution of the constraints at these different resolutions of the binary with parameters given in Table II. To track the constraint violations, we define $\mathcal{C} = \sum_\mu |(C_\mu)^2|/4$, and consider the global maximum $\max \mathcal{C}$ in each time-slice, as well as the integrated norm $\mathcal{I}_\mathcal{C} = \int d^3x \sqrt{\gamma} \mathcal{C}$. In Figure 18, we show the convergence behavior of the total $U(1)$ -charge of the system. Overall, the constraint violations converge to zero at the expected forth order of our numerical methods. The violation of the conservation of the $U(1)$ charge Q , shown in Figure 18, also converges towards zero. Likely, due

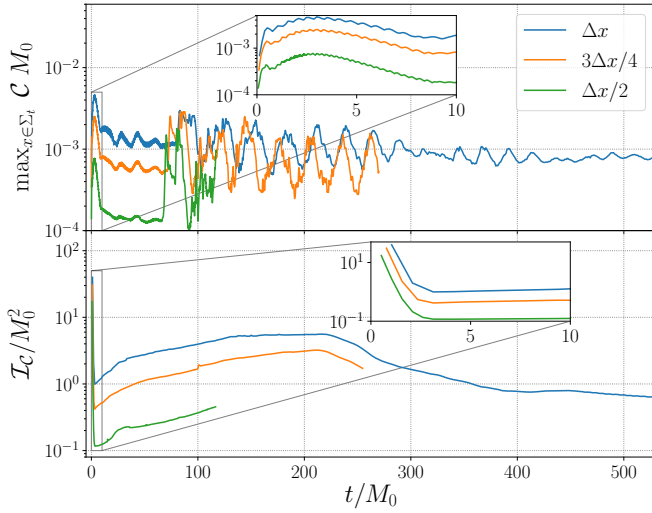


Figure 17. Here we consider the convergence behavior of the binary BS in the $\sigma = 0.05$ solitonic scalar model, with properties summarized in Table II, with decreasing grid spacing. The quantities \mathcal{C} and \mathcal{I}_C (defined in the text) are a positive definite measure of the constraint violation, which we track throughout the simulation. The rapid variation of the constraints is driven by gauge dynamics at early times. The maximum of the constraint violation \mathcal{C} occurs during the merger of the binary at around $t/M_0 \approx 75$. The binary merges earlier with increasing resolution, and only the medium and high resolutions capture small-scale features present in the remnant after merger. The quantity $\max \mathcal{C}$ converges to zero roughly at third order, as expected, since it is primarily set by the third-order accurate time interpolations on the mesh refinement boundaries. On the other hand, the integrated quantity \mathcal{I}_C converges at the expected fourth order, as it is largely insensitive to the lower-order time interpolations.

to the compactness ($C = 0.13$) of the BSs, rapid exponential decay of the scalar field outside the stars, i.e., $\Phi \sim \exp(-\sqrt{\mu^2 - \omega^2}r)$, with $\omega/\mu = 0.25$, and the large initial separation (of $D = 40M_0$), the low and medium resolutions exhibit relatively large drifts in the total conserved charge. Hence, the scalar field gradients on the surface of the stars, as well as the spatial scales of perturbations, require relatively high resolution.

Secondly, we discuss the numerical convergence of one of the binaries considered in Sec. IID. In particular, we focus on the $\alpha = \pi/2$ case, and compare its convergence behavior to that of the $\alpha = \pi$ binary evolution. In Figure 19, we present the convergence of the constraint violations with increasing resolution of the $\alpha = \pi/2$ evolution. Again, this demonstrates explicitly that we are solving the Hamiltonian and momentum constraints consistently within the $t = 0$ slice. In the subsequent evolution up to $t/M_0 = 100$, the constraints converge at the expected orders. For numerical stability purposes, we have to increase the size of the second coarsest mesh-refinement level in the lowest resolution run, moving the outer boundary of this level from $|x_i|/M_0 = 100$ to

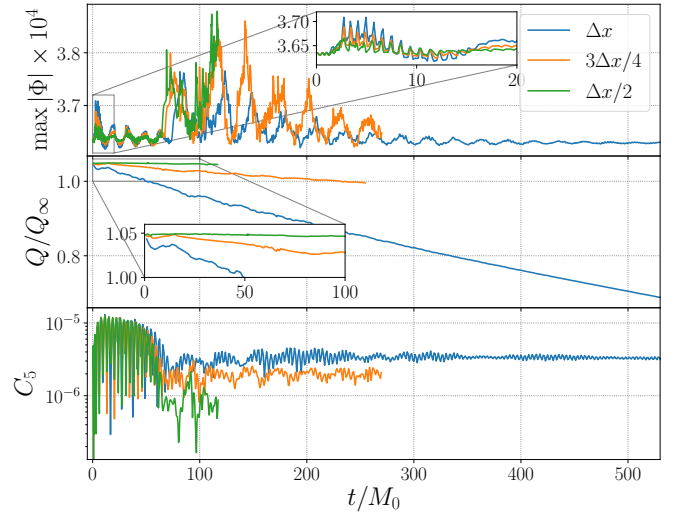


Figure 18. We consider the convergence behavior of the global maximum of $|\Phi|$, the total $U(1)$ -charge Q , and the azimuthal mode C_5 of the scalar field for the binary BS shown in Figure 17. The total charge Q is calculated in a coordinate sphere of radius $100M_0$ around the center of mass of the system. We normalize Q by Q_∞ , the sum of the BSs' isolated charges $Q_\infty = Q_1 + Q_2$. As the initial separation between the two stars increases, the total charge approaches the superposed charge [80]: $Q \rightarrow Q_\infty$. Lastly, we also show the convergence behavior of the C_5 mode [defined in (19)] during the binary evolution. The $m = 5$ perturbations remaining after the merger (and the formation of an $m = 1$ rotating remnant) at around $t/M_0 \approx 75$ are converging towards zero with increasing resolution at roughly the expected fourth order.

$|x_i|/M_0 \approx 241$. This explains the disagreement between the Δx and the $3\Delta x/4$ as well as $\Delta x/2$ resolutions in Figure 19, after $t/M_0 \approx 100$ (as at this time constraint violations propagating outward reach the mesh-refinement boundary in the medium and high resolution runs, but not yet in the low-resolution case). Furthermore, this different mesh-refinement layout in the low resolution case alters the convergence behavior, such that this case merges much earlier compared with the medium and high resolution runs. However, we have checked explicitly that the merger delay between the $\alpha = \pi/2$ and $\alpha = \pi$ cases *increases* from low (of $\Delta t/M_0 \approx 43$) to medium resolution evolutions (of $\Delta t/M_0 \approx 262$). Hence, the dephasing, delayed merger and black hole collapse discussed in Sec. IID are physical, and we are likely *underestimating* their impact on the GWs. Notice also, identical numerical setups were used for *all* cases presented Sec. IID, both for the initial data construction and evolution. Therefore, while *absolute* differences are not resolved, this is suggestive that the *relative* difference in amplitude in the GW waveform between the α -cases are driven by the scalar interactions, rather than numerical truncation error.

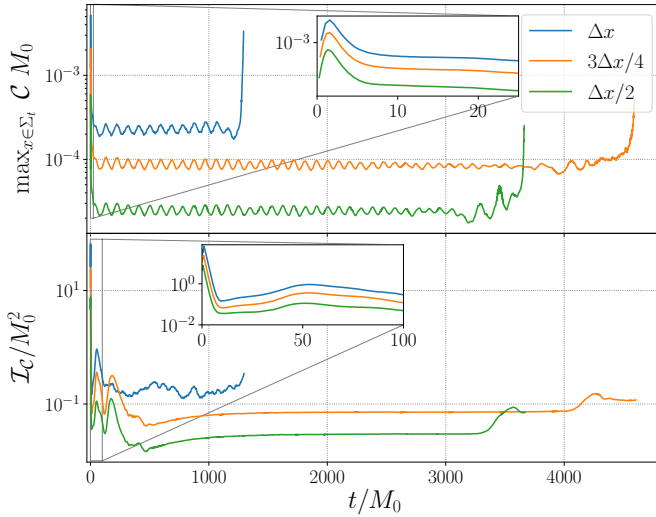


Figure 19. We consider the convergence behavior of the $\alpha = \pi/2$ case of Sec. II D with decreasing grid spacing Δx . The quantities C and I_C are defined in the text. The low resolution evolution is based on a different mesh-refinement layout (as discussed in the text,) and, hence, exhibits slightly different convergence behavior. At early times, the convergence orders of these quantities are the same as those discussed in the caption of Figure 17.

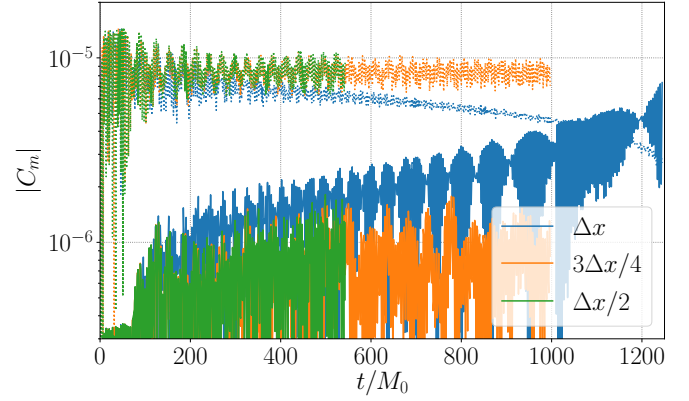


Figure 20. The evolution of the scalar field modes C_m (dotted and solid lines corresponding to $m = 1$ and 2 , respectively) defined in (19) for the binary BS merger specified in Table II with phase variation $\alpha/\pi = 63/64$. The merger occurs roughly at $t/M_0 \approx 75$, after which the even- m modes promptly begin to grow exponentially in the evolution with the *lowest* resolution (the $m = 0$ mode is representative of all even- m modes). This apparent instability is an artifact of low numerical resolution, and disappears with increasing resolution.

Appendix E: Vortex ejection as an artifact of numerical resolution

We find that in our simulations of the rotating BS formed from the merger of two non-rotating BS with a phase variation of $63/64 \geq \alpha/\pi \geq 7/8$ exhibit a growing perturbation leading to vortex ejection at low resolutions, but that this behavior disappears at sufficiently high resolution. In order to understand this behavior, it is instructive to consider an azimuthal mode decomposition of the real part of the scalar field, $\Phi_R = \text{Re}(\Phi)$, defined in (19). In Figure 20, we show the scalar field modes C_m during the merger of the binary BS specified in Table II with initial phase variation $\alpha/\pi = 63/64$. During, and shortly after, the merger around $t/M_0 = 75$, the $m = 1$ mode is the most dominant mode representing the formation of a $m = 1$ rotating BS, and indicating the formation of a $q = 1$ central vortex. Additionally, the amplitude of the even- m modes right after merger is consistent across resolutions. On the other hand, the even- m modes begin to grow exponentially right after formation of the rotating remnant (the representative $m = 0$ mode is shown in Figure 20) in the evolution with *lowest* resolution. Furthermore, we find that with increasing α , the amplitude of the even- m modes after merger decreases, but in all cases the artificial instability appears at lowest resolution; in fact, even in the $\alpha = \pi$ case, where the even- m modes are seeded at amplitudes consistent with floating point roundoff, we find this behavior. In all cases considered, this growing perturbation at low resolution saturates in the vortex ejection of the solution. However, we performed higher resolution evolutions in the binaries with $\alpha/\pi \in \{63/64, 31/32, 7/8\}$ and explicitly checked that the unstable behavior disappears. This is illustrated for $\alpha/\pi = 63/64$ in Figure 20.

-
- [1] V. Cardoso and P. Pani, *Living Rev. Rel.* **22**, 4 (2019), [arXiv:1904.05363 \[gr-qc\]](#).
- [2] R. L. Bowers and E. P. T. Liang, *Astrophys. J.* **188**, 657 (1974).
- [3] P. S. Letelier, *Phys. Rev. D* **22**, 807 (1980).
- [4] L. Herrera, A. Di Prisco, J. Martin, J. Ospino, N. Santos, and O. Troconis, *Phys. Rev. D* **69**, 084026 (2004), [arXiv:gr-qc/0403006](#).
- [5] S. D. Mathur, *Fortsch. Phys.* **53**, 793 (2005), [arXiv:hep-th/0502050](#).
- [6] I. Bena and N. P. Warner, *Lect. Notes Phys.* **755**, 1 (2008), [arXiv:hep-th/0701216](#).
- [7] V. Balasubramanian, J. de Boer, S. El-Showk, and I. Messamah, *Class. Quant. Grav.* **25**, 214004 (2008), [arXiv:0811.0263 \[hep-th\]](#).
- [8] V. Cardoso, S. Hopper, C. F. B. Macedo, C. Palenzuela, and P. Pani, *Phys. Rev. D* **94**, 084031 (2016), [arXiv:1608.08637 \[gr-qc\]](#).
- [9] J. L. Friedman, *Comm. Math. Phys.* **63**, 243 (1978).
- [10] D. J. Kaup, *Phys. Rev.* **172**, 1331 (1968).
- [11] R. Ruffini and S. Bonazzola, *Phys. Rev.* **187**, 1767 (1969).
- [12] E. Seidel and W.-M. Suen, *Phys. Rev. Lett.* **72**, 2516 (1994), [arXiv:gr-qc/9309015](#).
- [13] E. Seidel and W. M. Suen, *Phys. Rev. Lett.* **66**, 1659 (1991).
- [14] M. Alcubierre, R. Becerril, S. F. Guzman, T. Matos, D. Nunez, and L. A. Urena-Lopez, *Class. Quant. Grav.* **20**, 2883 (2003), [arXiv:gr-qc/0301105](#).
- [15] F. E. Schunck and E. W. Mielke, *Class. Quant. Grav.* **20**, R301 (2003), [arXiv:0801.0307 \[astro-ph\]](#).
- [16] S. L. Liebling and C. Palenzuela, *Living Rev. Rel.* **20**, 5 (2017), [arXiv:1202.5809 \[gr-qc\]](#).
- [17] L. Visinelli, *Int. J. Mod. Phys. D* **30**, 2130006 (2021), [arXiv:2109.05481 \[gr-qc\]](#).
- [18] R. Friedberg, T. Lee, and Y. Pang, *Phys. Rev. D* **35**, 3658 (1987).
- [19] J. Balakrishna, E. Seidel, and W.-M. Suen, *Phys. Rev. D* **58**, 104004 (1998), [arXiv:gr-qc/9712064](#).
- [20] F. E. Schunck and D. F. Torres, *Int. J. Mod. Phys. D* **9**, 601 (2000), [arXiv:gr-qc/9911038](#).
- [21] R. Sorkin, *Astrophys. J.* **249**, 254 (1981).
- [22] M. Gleiser, *Phys. Rev. D* **38**, 2376 (1988), [Erratum: *Phys. Rev. D* **39**, 1257 (1989)].
- [23] M. Gleiser and R. Watkins, *Nucl. Phys. B* **319**, 733 (1989).
- [24] T. Lee and Y. Pang, *Nucl. Phys. B* **315**, 477 (1989).
- [25] F. V. Kusmartsev, E. W. Mielke, and F. E. Schunck, *Phys. Rev. D* **43**, 3895 (1991), [arXiv:0810.0696 \[astro-ph\]](#).
- [26] F. Guzman, *Phys. Rev. D* **70**, 044033 (2004), [arXiv:gr-qc/0407054](#).
- [27] N. Sanchis-Gual, C. Herdeiro, and E. Radu, *Class. Quant. Grav.* **39**, 064001 (2022), [arXiv:2110.03000 \[gr-qc\]](#).
- [28] F. S. Guzman and L. A. Urena-Lopez, *Phys. Rev. D* **68**, 024023 (2003), [arXiv:astro-ph/0303440](#).
- [29] M. A. Amin and P. Mocz, *Phys. Rev. D* **100**, 063507 (2019), [arXiv:1902.07261 \[astro-ph.CO\]](#).
- [30] D. G. Levkov, A. G. Panin, and I. I. Tkachev, *Phys. Rev. Lett.* **121**, 151301 (2018), [arXiv:1804.05857 \[astro-ph.CO\]](#).
- [31] J. Veltmaat, J. C. Niemeyer, and B. Schwabe, *Phys. Rev. D* **98**, 043509 (2018), [arXiv:1804.09647 \[astro-ph.CO\]](#).
- [32] A. Arvanitaki, S. Dimopoulos, M. Galanis, L. Lehner, J. O. Thompson, and K. Van Tilburg, *Phys. Rev. D* **101**, 083014 (2020), [arXiv:1909.11665 \[astro-ph.CO\]](#).
- [33] C.-W. Lai, *A Numerical study of boson stars*, Other thesis (2004), [arXiv:gr-qc/0410040](#).
- [34] M. W. Choptuik and F. Pretorius, *Phys. Rev. Lett.* **104**, 111101 (2010), [arXiv:0908.1780 \[gr-qc\]](#).
- [35] A. Paredes and H. Michinel, *Phys. Dark Univ.* **12**, 50 (2016), [arXiv:1512.05121 \[astro-ph.CO\]](#).
- [36] A. Bernal and F. Siddhartha Guzman, *Phys. Rev. D* **74**, 103002 (2006), [arXiv:astro-ph/0610682](#).
- [37] B. Schwabe, J. C. Niemeyer, and J. F. Engels, *Phys. Rev. D* **94**, 043513 (2016), [arXiv:1606.05151 \[astro-ph.CO\]](#).
- [38] C. Palenzuela, I. Olabarrieta, L. Lehner, and S. L. Liebling, *Phys. Rev. D* **75**, 064005 (2007), [arXiv:gr-qc/0612067](#).
- [39] B. C. Mundim, *A Numerical Study of Boson Star Binaries*, Ph.D. thesis, British Columbia U. (2010), [arXiv:1003.0239 \[gr-qc\]](#).
- [40] M. Bezares, C. Palenzuela, and C. Bona, *Phys. Rev. D* **95**, 124005 (2017), [arXiv:1705.01071 \[gr-qc\]](#).
- [41] T. Helfer, U. Sperhake, R. Croft, M. Radia, B.-X. Ge, and E. A. Lim, (2021), [arXiv:2108.11995 \[gr-qc\]](#).
- [42] C. Palenzuela, L. Lehner, and S. L. Liebling, *Phys. Rev. D* **77**, 044036 (2008), [arXiv:0706.2435 \[gr-qc\]](#).
- [43] C. Palenzuela, P. Pani, M. Bezares, V. Cardoso, L. Lehner, and S. Liebling, *Phys. Rev. D* **96**, 104058 (2017), [arXiv:1710.09432 \[gr-qc\]](#).
- [44] M. Bezares, M. Bošković, S. Liebling, C. Palenzuela, P. Pani, and E. Barausse, *Phys. Rev. D* **105**, 064067 (2022), [arXiv:2201.06113 \[gr-qc\]](#).
- [45] M. Bezares and C. Palenzuela, *Class. Quant. Grav.* **35**, 234002 (2018), [arXiv:1808.10732 \[gr-qc\]](#).
- [46] R. Brito, V. Cardoso, C. A. R. Herdeiro, and E. Radu, *Phys. Lett. B* **752**, 291 (2016), [arXiv:1508.05395 \[gr-qc\]](#).
- [47] N. Sanchis-Gual, J. Calderón Bustillo, C. Herdeiro, E. Radu, J. A. Font, S. H. W. Leong, and A. Torres-Forné, (2022), [arXiv:2208.11717 \[gr-qc\]](#).
- [48] N. Sanchis-Gual, C. Herdeiro, J. A. Font, E. Radu, and F. Di Giovanni, *Phys. Rev. D* **99**, 024017 (2019), [arXiv:1806.07779 \[gr-qc\]](#).
- [49] F. Di Giovanni, N. Sanchis-Gual, C. A. R. Herdeiro, and J. A. Font, *Phys. Rev. D* **98**, 064044 (2018), [arXiv:1803.04802 \[gr-qc\]](#).
- [50] N. Sanchis-Gual, C. Herdeiro, E. Radu, J. C. Degollado, and J. A. Font, *Phys. Rev. D* **95**, 104028 (2017), [arXiv:1702.04532 \[gr-qc\]](#).
- [51] Y. Kobayashi, M. Kasai, and T. Futamase, *Phys. Rev. D* **50**, 7721 (1994).
- [52] F. Kling, A. Rajaraman, and F. L. Rivera, *Phys. Rev. D* **103**, 075020 (2021), [arXiv:2010.09880 \[hep-th\]](#).
- [53] B. Kleihaus, J. Kunz, and M. List, *Phys. Rev. D* **72**, 064002 (2005), [arXiv:gr-qc/0505143](#).
- [54] B. Kleihaus, J. Kunz, M. List, and I. Schaffer, *Phys. Rev. D* **77**, 064025 (2008), [arXiv:0712.3742 \[gr-qc\]](#).
- [55] N. Sanchis-Gual, F. Di Giovanni, M. Zilhão, C. Herdeiro, P. Cerdá-Durán, J. Font, and E. Radu, *Phys. Rev. Lett.* **123**, 221101 (2019), [arXiv:1907.12565 \[gr-qc\]](#).

- [56] F. Di Giovanni, N. Sanchis-Gual, P. Cerdá-Durán, M. Zilhão, C. Herdeiro, J. Font, and E. Radu, (2020), [arXiv:2010.05845 \[gr-qc\]](#).
- [57] N. Siemonsen and W. E. East, *Phys. Rev. D* **103**, 044022 (2021), [arXiv:2011.08247 \[gr-qc\]](#).
- [58] A. S. Dmitriev, D. G. Levkov, A. G. Panin, E. K. Pushnaya, and I. I. Tkachev, *Phys. Rev. D* **104**, 023504 (2021), [arXiv:2104.00962 \[gr-qc\]](#).
- [59] R. Croft, T. Helfer, B.-X. Ge, M. Radia, T. Evstafyeva, E. A. Lim, U. Sperhake, and K. Clough, (2022), [arXiv:2207.05690 \[gr-qc\]](#).
- [60] R. Friedberg, T. D. Lee, and A. Sirlin, *Phys. Rev. D* **13**, 2739 (1976).
- [61] S. R. Coleman, *Nucl. Phys. B* **262**, 263 (1985), [Addendum: *Nucl. Phys. B* 269, 744 (1986)].
- [62] M. Tsubota, K. Kasamatsu, and M. Ueda, *Phys. Rev. A* **65**, 023603 (2002).
- [63] J. Koplik and H. Levine, *Phys. Rev. Lett.* **71**, 1375 (1993).
- [64] W. F. Vinen, M. Tsubota, and A. Mitani, *Phys. Rev. Lett.* **91**, 135301 (2003).
- [65] K. W. Schwarz, *Phys. Rev. B* **38**, 2398 (1988).
- [66] R. P. Yu and M. J. Morgan, *Class. Quant. Grav.* **19**, L157 (2002).
- [67] P. Sikivie and Q. Yang, *Phys. Rev. Lett.* **103**, 111301 (2009), [arXiv:0901.1106 \[hep-ph\]](#).
- [68] B. Kain and H. Y. Ling, *Phys. Rev. D* **82**, 064042 (2010), [arXiv:1004.4692 \[hep-ph\]](#).
- [69] T. Rindler-Daller and P. R. Shapiro, *Mon. Not. Roy. Astron. Soc.* **422**, 135 (2012), [arXiv:1106.1256 \[astro-ph.CO\]](#).
- [70] T. W. B. Kibble, *J. Phys. A* **9**, 1387 (1976).
- [71] W. H. Zurek, *Nature* **317**, 505 (1985).
- [72] A. del Campo and W. H. Zurek, *Int. J. Mod. Phys. A* **29**, 1430018 (2014), [arXiv:1310.1600 \[cond-mat.stat-mech\]](#).
- [73] M. Bošković and E. Barausse, *JCAP* **02**, 032 (2022), [arXiv:2111.03870 \[gr-qc\]](#).
- [74] M. Axenides, S. Komineas, L. Perivolaropoulos, and M. Floratos, *Phys. Rev. D* **61**, 085006 (2000), [arXiv:hep-ph/9910388](#).
- [75] R. Battye and P. Sutcliffe, *Nucl. Phys. B* **590**, 329 (2000), [arXiv:hep-th/0003252](#).
- [76] P. Bowcock, D. Foster, and P. Sutcliffe, *J. Phys. A* **42**, 085403 (2009), [arXiv:0809.3895 \[hep-th\]](#).
- [77] S. Yoshida and Y. Eriguchi, *Phys. Rev. D* **55**, 1994 (1997).
- [78] C. A. R. Herdeiro, J. Kunz, I. Perapechka, E. Radu, and Y. Shnir, *Phys. Rev. D* **103**, 065009 (2021), [arXiv:2101.06442 \[gr-qc\]](#).
- [79] P. Cunha, C. Herdeiro, E. Radu, and Y. Shnir, (2022), [arXiv:2210.01833 \[gr-qc\]](#).
- [80] N. Siemonsen and W. E. East, (*in prep*).
- [81] E. Gourgoulhon, (2007), [arXiv:gr-qc/0703035](#).
- [82] K. Clough, *Class. Quant. Grav.* **38**, 167001 (2021), [arXiv:2104.13420 \[gr-qc\]](#).
- [83] R. Croft, (2022), [arXiv:2203.13845 \[gr-qc\]](#).
- [84] T. Evstafyeva, U. Sperhake, T. Helfer, R. Croft, M. Radia, B.-X. Ge, and E. A. Lim, (2022), [arXiv:2212.08023 \[gr-qc\]](#).
- [85] T. W. Baumgarte, S. L. Shapiro, and M. Shibata, *Astrophys. J. Lett.* **528**, L29 (2000), [arXiv:astro-ph/9910565](#).
- [86] S. Bernuzzi, T. Dietrich, W. Tichy, and B. Brügmann, *Phys. Rev. D* **89**, 104021 (2014), [arXiv:1311.4443 \[gr-qc\]](#).
- [87] K. A. Çokluk, K. Yakut, and B. Giacomazzo, (2023), [arXiv:2301.09635 \[astro-ph.HE\]](#).
- [88] G. Moschidis, *Commun. Math. Phys.* **358**, 437 (2018), [arXiv:1608.02035 \[math.AP\]](#).
- [89] A. Hook and J. Huang, *JHEP* **06**, 036 (2018), [arXiv:1708.08464 \[hep-ph\]](#).
- [90] J. Huang, M. C. Johnson, L. Sagunski, M. Sakellariadou, and J. Zhang, *Phys. Rev. D* **99**, 063013 (2019), [arXiv:1807.02133 \[hep-ph\]](#).
- [91] J. Zhang, Z. Lyu, J. Huang, M. C. Johnson, L. Sagunski, M. Sakellariadou, and H. Yang, *Phys. Rev. Lett.* **127**, 161101 (2021), [arXiv:2105.13963 \[hep-ph\]](#).
- [92] M. J. Thatcher and M. J. Morgan, *Classical and Quantum Gravity* **14**, 3161 (1997).
- [93] C. Herdeiro, I. Perapechka, E. Radu, and Y. Shnir, *Phys. Lett. B* **797**, 134845 (2019), [arXiv:1906.05386 \[gr-qc\]](#).
- [94] W. E. East, F. M. Ramazanoglu, and F. Pretorius, *Phys. Rev. D* **86**, 104053 (2012), [arXiv:1208.3473 \[gr-qc\]](#).
- [95] J. W. York, Jr., *Phys. Rev. Lett.* **82**, 1350 (1999), [arXiv:gr-qc/9810051](#).
- [96] M. Corman and W. E. East, (2022), [arXiv:2212.04479 \[gr-qc\]](#).
- [97] F. Pretorius, *Class. Quant. Grav.* **22**, 425 (2005), [arXiv:gr-qc/0407110 \[gr-qc\]](#).
- [98] W. E. East, F. Pretorius, and B. C. Stephens, *Phys. Rev. D* **85**, 124010 (2012), [arXiv:1112.3094 \[gr-qc\]](#).
- [99] L. Lindblom and B. Szilagyi, *Phys. Rev. D* **80**, 084019 (2009), [arXiv:0904.4873 \[gr-qc\]](#).